Thesis

An observational and theoretical investigation of the evolution of biomass–burning aerosol size distributions

Submitted by

Kimiko M. Sakamoto

Department of Atmospheric Science

In partial fulfillment of the requirements

For the Degree of Master of Science

Colorado State University

Fort Collins, Colorado

Spring 2015

Master's Committee:

Advisor: Jeffrey Pierce

Sonia Kreidenweis
John Volckens

Abstract

An observational and theoretical investigation of the evolution of biomass–burning aerosol size distributions

Biomass-burning aerosols contribute to aerosol radiative forcing on the climate system. The magnitude of this effect is partially determined by aerosol size distributions, which are functions of source fire characteristics (e.g. fuel type, MCE) and in-plume microphysical processing (occurring on a GCM sub-grid scale). The uncertainties in biomass-burning emission number size-distributions in climate model inventories lead to uncertainties in the CCN concentrations and forcing estimates derived from these models. This uncertainty emphasizes the need for observational and modelling studies to better represent effective biomass-burning size-distributions in larger-gridbox models.

The BORTAS-B measurement campaign was designed to sample boreal biomass-burning outflow over Eastern Canada in the summer of 2011. Using these BORTAS-B data, we implement plume criteria to isolate the characteristic size-distribution of aged biomass-burning emissions (aged $\sim$1 – 2 days) from boreal wildfires in Northwestern Ontario. The composite median size distribution yields a single dominant accumulation mode with D_{pm}= 230 nm (number-median diameter), σ= 1.5, which are comparable to literature values of other aged plumes of a similar type. The organic aerosol enhancement ratios (ΔOA/ΔCO) along the path of Flight b622 show values of 0.05-0.18 μg m^{-3}ppbv^{-1} with no significant trend with distance from the source. This lack of enhancement ratio increase/decrease with distance suggests no detectable net OA production/evaporation within the aged plume over the sampling period.

A Lagrangian microphysical model was used to determine an estimate of the freshly emitted size distribution and flux corresponding to the BORTAS-B aged size-distributions. The model was restricted to coagulation and dilution processes only based on the insignificant net OA production/evaporation derived from the ΔOA/ΔCO enhancement ratios. We estimate that the fresh-plume median diameter was in the range of 59-94 nm with modal widths in

the range of 1.7-2.8 (the ranges are due to uncertainty in the entrainment rate). Thus, the size of the freshly emitted particles is relatively unconstrained due to the uncertainties in the plume dilution rates.

Expanding on the fresh-plume coagulational modelling of the BORTAS-B plumes, a coagulation-only parameterization for effective biomass-burning size-distributions was developed using the SAM-TOMAS plume model and a gaussian emulator. Under a range of biomass-burning conditions, the SAM-TOMAS simulations showed increasing D_{pm} and decreasing σ (converging to 1.2) with distance from the emission source. Final D_{pm} also shows a strong dependence on dM/dx (Mass flux $\times$ Fire area/v_g), with larger values resulting in more rapid coagulation and faster dD_{pm}/dt.

The SAM-TOMAS simulations were used to train the Gaussian Emulation Machine for Sensitivity Analysis (GEM-SA) to build a D_{pm} and σ parameterization based on seven inputs. The seven inputs are: emission D_{pm_0}, emission σ_0, mass flux, fire area, mean boundary layer wind (v_g), time, and plume mixing depth (d_{mixing}). These inputs are estimated to account for 81% of the total variance in the final size distribution D_{pm}, and 87% of the total variance in the final σ. The parameterization performs very well against non-training modelled SAM-TOMAS size-distributions in both final D_{pm} (slope = 0.92, R^2 = 0.83, MNB=-0.06) and final σ (slope = 0.91, R^2= 0.93, MNB = 0.01). These final size distribution parameters are meant to be inserted as effective biomass-burning aerosol size-distributions (single lognormal mode) into larger-scale atmospheric models.

Acknowledgements

I would firstly like to thank Dr. Jeffrey Pierce for his help and guidance, which extended from the very beginning stages of this project right through to the end. Without such advice and enthusiasm, this project would not have come together as it did. I would also like to extend my gratitude to Dr. Sonia Kreidenweis and Dr. John Volckens for joining as members of my committee.

I am indebted to Dr. Robin Stevens for his extensive contributions in helping me set up both the SAM-TOMAS model and the Gaussian emulator. I would also like to thank Dr. Ezra Levin for teaching me how to operate an SMPS, and the Kreidenweis lab for allowing me the privilege of doing so in their lab. I would also like to acknowledge Dr. Thomas Duck at the Dalhousie University, without whom I would likely have never become involved with the BORTAS-B campaign (or atmospheric science) in the first place.

Not enough can be said of the numerous individuals involved in planning and executing the BORTAS-B campaign of 2011, as well as those involved in the data filtering and processing post-campaign. I would especially like to thank Dr. James Allen, Dr. Hugh Coe, and Mr. Jonathan Taylor of the University of Manchester for the use of the size-distribution, black carbon, and AMS data, as well as the numerous e-mail discussions concerning them. The University of East Anglia provided the PTR-MS VOC data. Additional BORTAS-B flight data and CO measurements used in this project were made available by FAAM.

Finally, I need to thank Steve D'Andrea, Landan MacDonald, Jack Kodros, Bonne Ford and the rest of the extended Pierce group for their support, discussions, company, and coffee. Funding for this project was provided in part from the Joint Fire Science Program under Project JFSP 13-1-01-4.

Table of Contents

List of Figures

List of Tables

List of Symbols and Abbreviations

AMS	Aerosol mass spectrometer
ARA	Atmospheric research aircraft run by FAAM for BORTAS-B
BB	Biomass burning
BC	Black carbon
BORTAS-B	Quantifying the impact of boreal forest fires on the tropospheric oxidants over the Atlantic using aircraft and satellites, B-phase
CCN	Cloud condensation nuclei
CH_3CN	Acetonitrile
CO	Carbon monoxide
d_{mixing}	Aerosol plume mixing depth, [m]
D_{pm_0}	Emission median diameter of a lognormal size distribution
D_{pm}	Median diameter of a lognormal size distribution
dM/dx	Mass in an infinitesimally thin slice of air (normal to the mean wind, v_g), [kg m^{-1}]
$\Delta OA/\Delta CO$	Organic aerosol enhancement ratio, [μg m^{-3}ppbv^{-1}]
FLAME	Fire lab at Missoula experiment
MODIS	Moderate resolution imaging spectroradiometer
N_0	Total particle number (as concentration cm^{-3})
MNB	Mean normalized bias
OA	Organic aerosol
POA	Primary organic aerosol
σ_0	Emission modal width of lognormal size distribution mode
σ	Modal width of a lognormal size distribution mode
SMPS	Scanning mobility particle sizer
SOA	Secondary organic aerosol
τ_{dil}	e-folding volume exchange (dilution) exponent
v_g	mean boundary layer windspeed, SAM-TOMAS wall speed
VOC	Volatile organic compound

1. Introduction[1]

1.1 Biomass-burning particles

Biomass burning is a significant emission source of carbonaceous aerosols to the global atmosphere (Andreae and Merlet, 2001; Reid et al., 2005). In addition to releasing high levels of greenhouse gases (CO_2, CO) and volatile organic compounds, biomass burning releases smoke particles that have climate impacts through the direct and indirect aerosol effects. These particles are primarily composed of a mixture of black carbon and organic carbon, with inorganics contributing some mass (Capes et al., 2008; Carrico et al., 2010; Cubison et al., 2011; Hecobian et al., 2011; Hennigan et al., 2011; Hudson et al., 2004; Reid et al., 2005). These particles directly affect the earth's radiation balance and climate by scattering and absorbing incoming solar radiation directly (Boucher, 2000; Jacobson, 2001). Biomass burning particles may also act as cloud condensation nuclei (CCN) and affect climate and radiation through modifying cloud albedo and lifetime (Pierce et al., 2007; Spracklen et al., 2011) (indirect aerosol effects). Globally, the direct and indirect climate effects, to which biomass-burning aerosols contribute, represent the largest uncertainties in radiative forcing as quantified by the recent IPCC report (Myhre et al., 2013), and biomass burning emissions represent significant contributions to each of the effects globally (Alonso-Blanco, 2014; Lee et al., 2013).

The size of biomass-burning particles (and all particles in general) can have large impacts on the magnitude of these direct and indirect effects (Lee et al., 2013; Seinfeld and Pandis, 2006; Spracklen et al., 2011). Regarding the direct effect, the mass-scattering and mass-absorption efficiencies (the amount of scattering and absorption per mass of aerosol particles) depend on the size of the particles, so errors in the predicted/assumed values of biomass-burning particle size may lead to errors in simulated direct aerosol climate effects (Seinfeld and Pandis, 2006). Regarding the indirect effect, particles that are larger in diameter and

[1]Modified introduction from Sakamoto, K. M., Allan, J. D., Coe, H., Taylor, J. W., Duck, T. J., and Pierce, J. R.: Aged boreal biomass burning aerosol size distributions from BORTAS 2011, Atmos. Chem. Phys. Discuss., 14, 24349-24385, doi:10.5194/acpd-14-24349-2014, 2014. (in review). Ownership is retained by the authors: www.atmospheric-chemistry-and-physics.net/general_ information/license_ and_ copyright.html

more hygroscopic are more likely to act as CCN (Petters and Kreidenweis, 2007). Typically particles larger than 30-100 nm act as CCN depending on conditions and hygroscopicity (Petters and Kreidenweis, 2007; Petters et al., 2009), though this range may be slightly larger for fresh biomass burning particles due to these particles being initially more hydrophobic than typical ambient aerosol (Carrico et al., 2010; Petters and Kreidenweis, 2007).

Furthermore, for constant emissions mass, a factor-of-2 change in diameter leads to a factor-of-8 change in number emissions. Spracklen et. al., (2011) modelled the particle size sensitivity of the 1st aerosol indirect effect (albedo) using carbonaceous combustion aerosol. Lee et al. (2013) found that uncertainties in biomass-burning aerosol emission diameter were responsible for large uncertainties in CCN concentrations in the GLOMAP model (third largest CCN sensitivity out of 28 globally). This study, and other CCN modelling studies like it, emphasize the potential contribution of particle size to significant changes in modelled CCN concentrations, leading to changes in estimated climate effects (Pierce et al., 2007). Therefore, it is important to provide accurate emissions sizes from biomass burning sources to atmospheric aerosol models looking at aerosol-climate interactions.

Atmospheric processing causes the physical and chemical properties of biomass-burning (BB) aerosol to evolve over time. These processes have an effect on the size and composition of the particles, and thus influence their direct and indirect effects. Coagulation is a driving factor in size-distribution evolution due to the high concentrations of particles within plumes (Andreae and Merlet, 2001; Capes et al., 2008). Production of secondary organic aerosol (SOA) in-plume has been observed in chamber studies (Cubison et al., 2011; Grieshop et al., 2009; Hennigan et al., 2011; Heringa et al., 2011; Ortega et al., 2013) and in the field (DeCarlo et al., 2010; Lee et al., 2008; Reid et al., 1998; Yokelson et al., 2009), and this SOA will condense onto the particles growing them to larger sizes. In addition, the primary organic aerosol (POA) emitted by the fires may evaporate during the dilution of the plume (Hennigan et al., 2011). Finally, new particle formation in smoke plumes has been observed in smog chamber studies (Hennigan et al., 2012) as well as in the field (Andreae et al., 2001; Hobbs et al., 2003; Rissler et al., 2006).

In global and regional modelling of biomass-burning aerosols, mass-based biomass-burning inventories are the standard, and are often not accompanied by size data (Reid et al., 2009; van der Werf et al., 2010; Wiedinmyer et al., 2011), leaving size-distribution estimates to the individual investigator. Current global and regional atmospheric aerosol models have grid-box spatial scales (10s-100s of kms) much larger than many initial biomass-burning plume widths (<10 km). This means that sub-grid aging of aerosol plumes by microphysical (coagulation, condensation/evaporation and nucleation) processes will lead to changes in the size distribution that the models cannot explicitly resolve. Therefore, the biomass-burning emissions size distributions must be aged distributions that already account for sub-grid processes.

Quantifying the natural variations in biomass-burning aerosols are therefore necessary for accurate predictions. Previous studies of field and lab experiments show biomass burning size-distributions vary according to plume age, combustion phase, and fuel type (Hennigan et al., 2011; Hosseini et al., 2010; Janhäll et al., 2010; McMeeking et al., 2009; Okoshi et al., 2014). A review of observed size distribution data by Janhäll et al.(2010) showed the differences in modal width and median diameter as a function of fuel type (forest, savannah, grass), modified combustion efficiency, and plume age (fresh versus aged). Smog chamber experiments in the FLAME lab have demonstrated similar fuel-type differences in fresh BB size-distributions (Levin et al., 2010).

Due to the combination of emission and atmospheric processing factors contributing to the evolution of the BB aerosol size-distribution, characterization of observed, aged BB aerosol is invaluable. Adding to the database of observations helps constrain the uncertainties associated with aerosol size. Thus, to improve biomass-burning-aerosol/climate interactions in models, there is a need to characterize the size of particles in aging and aged biomass-burning plumes for a range of fire types and atmospheric conditions (Bauer et al., 2010; Chen et al., 2010; Lee et al., 2013; Pierce et al., 2007; Reddington et al., 2011; Spracklen et al., 2011).

In Chapter 2 of this study we specifically investigate the size distributions measured in aged plumes (1–2 days) of large boreal forest fires over Canada. We analyse the plume organic aerosol enhancement ratios and attempt to model the associated fresh plume distributions. In Chapter 3, we use a regional plume model to build a coagulation-only BB size distribution parameterization to capture the behaviour of BB aerosol size with time. We further investigate the behaviour of the modelled size-distributions with sensitivity analysis. This parameterization was built with the goal of furnishing effective biomass-burning size-distributions for use in atmospheric models based on available model and inventory input parameters.

2. Aged boreal biomass burning size distributions from BORTAS 2011[2]

2.1 Objectives

In this chapter we analyze size-distribution and organic aerosol data from select BORTAS-B flights that sampled highly concentrated smoke plumes over Eastern Canada on July 20-21st, 2011. This was done with the goal of adding to the body of scientific literature of observed, aged, boreal BB size-distributions. Organic aerosol enhancement analysis is also presented to better characterize the sampled plumes. In addition to observational data, we use an aerosol-microphysics box model to simulate the microphysical evolution of number size-distributions. This model was employed to estimate the fresh-plume size distribution associated with the source fires sampled during BORTAS-B.

A brief overview of the BORTAS-B campaign, instrumentation, and source fire conditions are provided in Section 2.2.1-2.2.2. A description of the quantitative plume criteria used to determine plume (versus out of plume) sampling periods is found in Section 2.2.3. A full box-model description is provided in Section 2.2.4. We present the BORTAS-B research flight results in Section 2.3, which include the measured aged size distributions, evidence for/against net OA production, and the aging simulations. Finally, we provide our conclusions to the study in Section 2.4.

2.2 Experimental Methods

2.2.1 BORTAS overview

The *Quantifying the impact of BOReal forest fires on the Tropospheric oxidants over the Atlantic using Aircraft and Satellites* (BORTAS-B) measurement campaign was held in Eastern/Atlantic Canada from July 11 - August 3, 2011 (Palmer et al., 2013). The goal was to characterize pyrogenic outflow from boreal forest wildfires using a variety of sampling and

[2]Sections 2.2-2.4 of this chapter are currently in review: Sakamoto, K. M., Allan, J. D., Coe, H., Taylor, J. W., Duck, T. J., and Pierce, J. R.: Aged boreal biomass burning aerosol size distributions from BORTAS 2011, Atmos. Chem. Phys. Discuss., 14, 24349-24385, doi:10.5194/acpd-14-24349-2014, 2014. Ownership is retained by the authors: www.atmospheric-chemistry-and-physics.net/general_ information/license_ and_ copyright.html

observational techniques with emphasis on plume photochemical evolution. BORTAS-B was the second phase of a collaborative effort between UK and Canadian groups after a less intensive BORTAS-A campaign took place over the same geographical area in 2010 (Palmer et al., 2013).

BORTAS-B incorporated predictive chemical transport modelling (GEOS-Chem), satellite observations, a ground-based in-situ network of sondes (Environment Canada) and ground-base samplers and profilers (Dalhousie Ground Station, DGS), and the UK Facility for Airborne Atmospheric Measurements Airborne Research Aircraft (FAAM-ARA) for inflight sampling. For a complete overview of the BORTAS-B set-up and instrumentation, see Palmer et al., (2013).

The ARA flew fourteen research flights over the campaign period. The flight paths of the ARA flights that we analyze in this paper can be seen in Figure 2.1. Flights BAE-b622 and BAE-b623 were research flights between Halifax, NS and Sherbrooke, QB spanning July 20-21, 2011. They flew ascent and descent patterns (ranging $\sim$1-7 km ASL) to sample vertical and horizontal transects in regions forecasted to contain biomass-burning plumes. These flights were selected because they were roughly co-located and back-to-back, increasing the likelihood of sampling similar outflow and allowing for a common plume criteria to be applied across both flights. They also contained the majority of biomass-burning aerosol sampling during the campaign.

In addition, Flight b622 sampled along a relatively straight path to/from the fires that allowed for analysis of the evolution of plume aerosol properties (Flight b623 had a much more complicated and compact sampling path so we did not use this flight to determine the evolution of aerosol properties). We have divided these flights into vertical transects by ascent/descent with the midpoints transect represented in Figure 2.1.

The sampled wildfire plumes originated from intense regional fires near the Northwestern Ontario-Manitoba border (centred 52°N, 93°W). The MODIS hotspots in Figure 2.1 show a number of intense fires (fire radiative power >100 MW) in northwestern Ontario for the three days prior to the analyzed flights (June 17-20, 2011). According to the Ontario Ministry

of Natural Resources, Ontario experienced one of its worst fire seasons in terms of burned area with 635,374 hectares burned in 2011 (Ontario Ministry of Natural Resources and Forestry, 2012). This is significantly greater than the acreage burned in 2010 during the BORTAS-A campaign (15,000 hectares). The abundance of individual fires in a relatively large source region lead to mixed combustion phases and dominant hotspots over the course of the campaign. A combination of flaming and smouldering phases were reported by Natural Resources Canada with primary fuels consisting of jack pine (*pinus banksiana*) and black spruce (*picea mariana*) throughout the fire region (Ontario Ministry of Natural Resources and Forestry, 2012).

The dominant west-east climatological meteorology during the BORTAS-B campaign allowed the biomass-burning emissions from these fires to be transported downwind over the ground-base, DGS, in Halifax, NS (44.5°N, 63.1°W). The plumes intersected by flights

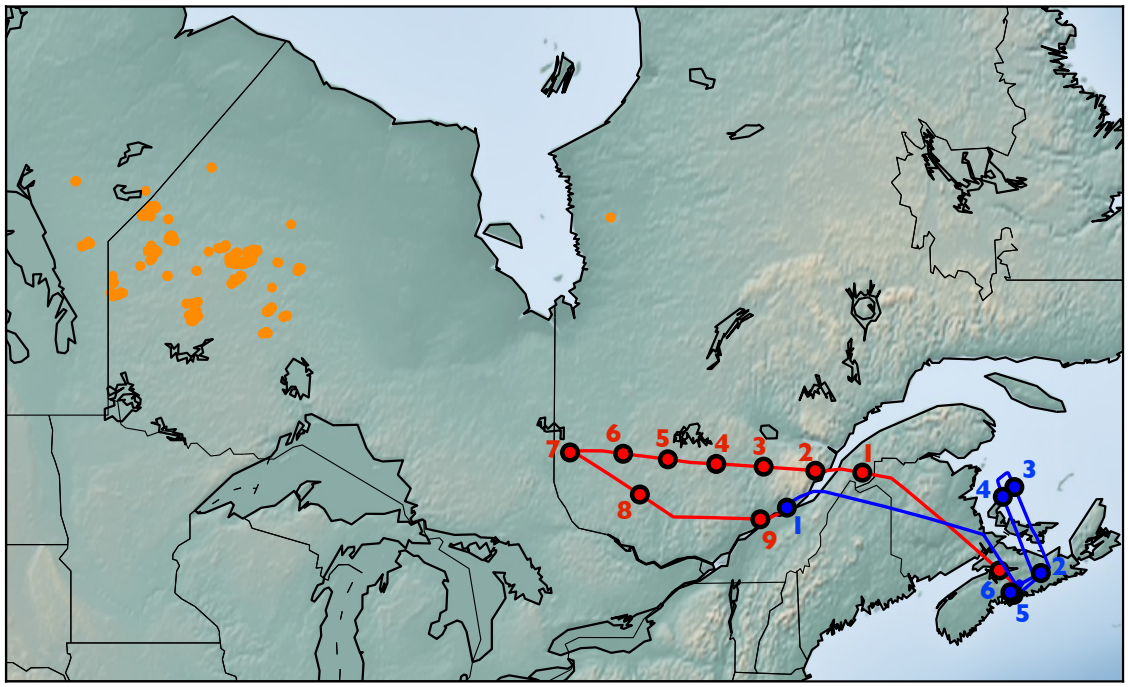

FIGURE 2.1. BORTAS-B ARA research flights b622 (red) from Nova Scotia to Quebec, and the return flight b623 (blue) both on July 20-21, 2011. Circles represent midpoints of ascent/descent transects along the flight paths and are numbered in sequence. The ARA flew through biomass-burning emissions originating from fires in Northwestern Ontario. The July 17-20, 2011 MODIS hotspot fires (frp >100 MW) are plotted in orange.

TABLE 2.1. Approximate physical transport age and distance of numbered flight transect midpoints from source fires. Ages were estimated by HYSPLIT back trajectories. The large ranges in the determined values are due to the large extent of the source fire region and variability in fire conditions. The distances are given from transect midpoints to the source fire region (± 150 km).

Transect Number	*Approx. physical Age [hrs]*	*Approx. distance from source [km]*
Flight b622		
1	27 - 32	1450 - 1750
2	27 - 32	1350 - 1650
3	27 - 32	1250 - 1550
4	27 - 32	1150 - 1450
5	18 - 25	1050 - 1350
6	18 - 25	850 - 1150
7	18 - 25	850 - 1150
8	18 - 25	1050 - 1350
9	24 - 30	1350 - 1650
Flight b623		
1	24 - 36	1350 - 1650
2	28 - 36	2050 - 2350
3 - 4	28 - 36	1850 - 2150
5 - 6	28 - 36	1950 - 2250

b622 and b623 had a physical transport age estimated through HYSPLIT backtrajectories of between 1-2 days as summarized in Table 2.1. Trajectory analysis shows air masses passing over the biomass-burning region later being intersected by the flight paths (Append. A.1). The estimated photochemical age of the plumes, based on non-methane hydrocarbon analysis via Parrish et al. (2007) was calculated by Palmer et al. (2013) to be 1-5 days for b622 and 2-4 days for b623; however, this differs from the physical transport age due to the photochemical age including the photochemical age of the air mixed into the plume.

2.2.2 ARA Instrumentation

The ARA aircraft was outfitted with instruments designed for sampling chemical and physical characteristics of biomass-burning outflow. Gaseous and particulate in-flight sampling was accomplished across a suite of instruments; the relevant instruments for this study are described below. A full description of all payload instruments can be found in (Palmer et al., 2013).

The suite of instruments on the ARA included measurements of multiple gaseous biomass-burning tracers. Carbon monoxide (CO) mole fraction was measured via VUV Fast fluorescence CO analyzer averaged over 1s (3% estimated accuracy). Acetonitrile (CH_3CN), a biomass-burning marker VOC associated with plant pyrolysis, was measured along with a number of other VOCs with a proton-transfer-reaction mass spectrometer (PTR-MS) system (co: University of East Anglia). The PTR-MS concentrations were averaged over 1s with an estimated precision of ± 37 ppt (Palmer et al., 2013).

Aerosol composition measurements used here were taken by i) refractory black carbon (BC) mass and number measurements from a Single Particle Soot Photometer (SP2) (accuracy 20%, precision 5%, 5s averaging time) and ii) non-refractory organic aerosol (OA) via an aerosol mass spectrometer (precision ∼15-150 ng m^{-3}) both operated by the University of Manchester (Taylor et al., 2014). The number concentrations of the combined aerosol particles was measured by Scanning Mobility Particle Sizer (SMPS) with 26 lognormally-spaced diameter bins ranging from 20-330 nm (60 second scans) and corrected to STP (Palmer et al., 2013). The SMPS data was inverted using the commonly-used Wiedensohler (1988) parameterisation, however recent work has suggested that this may be quantitatively unreliable in this situation due to variations in the charging efficiency with pressure (López-Yglesias and Flagan, 2013; Leppä et al., 2014). While this may have affected the magnitude of the number concentrations, no altitude dependency was noted in the sizing data, so the conclusions of this study regarding particle size are unaffected.

The combination of gas and particle tracer measurements listed above were used to identify flight periods of biomass-burning plume sampling, determine if SOA formation or OA evaporation may have occurred in the plume, and characterize the size-distribution of aerosols within the plume.

2.2.3 Plume Criteria

We determine if measurements are in-plume versus out-of-plume using threshold plume criteria. We designate sampling periods as in-plume if pre-specified threshold values of four

tracer species: CO, CH_3CN, BC, and OA, were exceeded. For out-of-plume conditions, we determine background values for each tracer by averaging the tracers over the out-of-plume periods.

Carbon monoxide (τ_{CO} ~months (Staudt et al., 2001)) and acetonitrile (τ_{ace} ~6 months (Holzinger et al., 2005)) were used in conjunction as gaseous tracers due to their high mixing ratios in biomass-burning plumes relative to the background and long atmospheric lifetimes relative to the estimated plume transport times. The background CO levels were 80-120 ppbv with an overall average of 100 ppbv. The threshold CO value was set to 150 ppbv (1.5

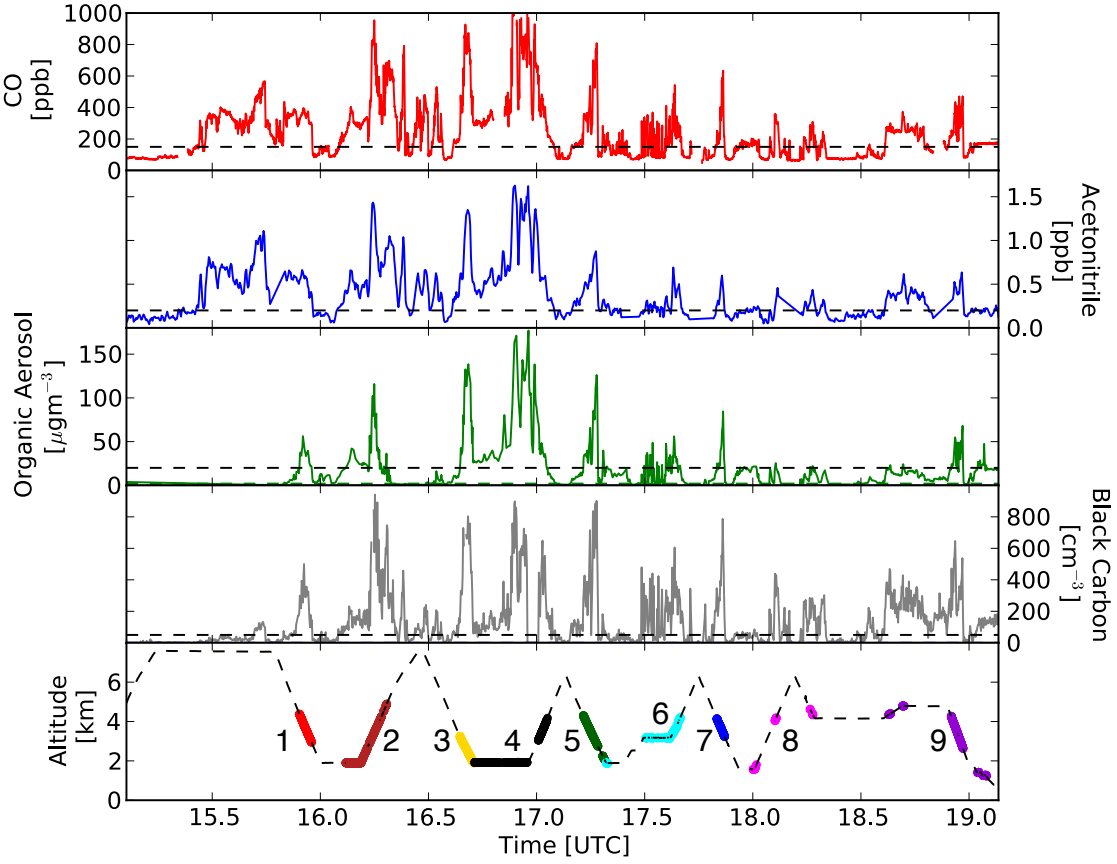

FIGURE 2.2. Time series of BORTAS-B aircraft measurements of biomass-burning tracer species for Flight b622. Threshold values were used across four species as plume criteria: i) CO (red, threshold = 150 ppb), ii) Acetonitrile (blue, threshold = 200 pptv), iii) Organic aerosols (green, mass threshold= 20 μg m^{-3}, at STP), iv) Black carbon (grey, number threshold = 50 cm^{-3}, at STP). The bottom panel shows flight altitude with plume sampling periods coloured. The plume data is further divided into transects (1-9 in red-violet).

× [background]), with some CO concentrations in-plume reaching ten times background concentrations (1000 ppbv). The threshold CH_3CN level was 200 pptv (background ∼100 pptv).

The particulate matter thresholds (BC number, OA mass) were introduced to ensure high-enough aerosol contributions to the plume to analyze size-distributions. This ensured high-gas, low-aerosol sampling periods were not included in the size-distribution analysis. At least one case of this situation in BORTAS-B has been attributed by Franklin et al. (2014) to aerosol rainout during transport. The mean background concentrations for both BC number and OA mass were minimal (<20 cm^{-3} and 2 $\mu g\ m^{-3}$ respectively). The threshold values were set to 50 cm^{-3} for BC number and 20 $\mu g\ m^{-3}$ for OA mass.

The selected CO, CH_3CN, aerosol data, and flight altitude time series for Flight b622 is shown in Figure 2.2. The flight is divided into transects (labeled 1-9 and colored) as seen in the altitude plot (Figure 2.2, bottom). We use these in-plume time periods to differentiate between in-plume and background aerosols throughout the paper. The time series for Flight b623 shows similar in-plume durations for the same criteria thresholds (Append. A.2).

2.2.4 Model Description

We use a Lagrangian box model to simulate the evolution of the biomass-burning size distribution due to coagulation. The model has fifty-five lognormally distributed size bins that correspond to the size bins of the SMPS on the ARA and extend to both larger and smaller diameters. The model includes coagulation and dilution as the only physical processes, with no chemistry or speciation of the aerosol (we show in Section 2.3.2 that we cannot see evidence of net OA condensation/evaporation in the plume). We use an inverse method to estimate the initial fresh (∼1 hour) number size-distributions by successively running the model from emission to observation forward in time and changing the initial size distribution until the model most closely matches the observed aged size distribution. This method estimates the initial distribution assuming that coagulation was the only physical processes affecting the in-plume particles. The box model does not include any cloud interaction chemistry, which

could have influenced the distribution considerably depending on meteorological conditions, notably through wet deposition and aqueous chemistry.

Each model forward simulation requires the fresh size-distribution input as a single log-normal mode with parameters: median diameter (D_{pm}), modal width (σ), and particle number (N_0). We use the brownian coagulation kernel (K_{ij}) of Fuchs (1964) to calculate the coagulation rate (Append A.3).

Dilution of the plume in transport was modelled using a simple e-folding volume mixing time, τ_{dil}. This parameter controlled the entrainment during each timestep between the in-plume and background aerosol. The rate of plume dilution may significantly affect the rate of coagulation throughout the simulation (the coagulation rate is proportional to N^2). Different values of τ_{dil} were tested to account for a range of entrainment rates as the dilution rate in the plume is relatively unconstrained. We test τ_{dil} values of 24, 36 and 48 hours. The 36 hr dilution rate was based on an estimate of volume expansion from Gaussian plume equations with an initial plume width of 10 km in a neutral stability environment (Klug, 1969). The range (24 - 48 hrs) accounts for atmospheric stability and plume width variations in the BORTAS source region. The model simulation time is 48 hours based on the upper age limits shown in Table 2.1.

To determine the best estimate for initial conditions, we simulate a range of fresh plume parameters: median diameter, D_{pm}, modal width, σ, and number, N_0. The input median diameter range was between 60-120 nm (increment = 1 nm), with σ ranging from 1.0-2.5 (increment = 0.1) and N_0 ranging from 5,000 – 150,000 cm^{-3} (increment = 500 cm^{-3}). The parameter space was optimized by brute force (i.e. every combination of input parameters was simulations) for each set dilution time and the final modelled size-distribution was compared to the observed in-plume size distribution by an equally weighted objective function. The objective function used was the sum of the absolute residual across the SMPS range. Modelled data outside of the SMPS size range was not used in the objective function.

2.3 Results

2.3.1 Observed size distributions

Observed SMPS size-distributions for individual plume transects showed highly elevated particle counts with little variation between transects and flights. The transect-divided data for Flight b622 are shown in Figure 2.3. Transects 2-6 and 9, show a clearly elevated accumulation mode within the plume, with a peak median diameters of 180-240 nm. Transects 1, 7 and 8 have significantly less data (<3 data points per size bin) due to the lesser in-plume sampling periods (incomplete SMPS scans).

Those transects with sufficient plume data (<3 data points per bin) are plotted against their accumulation mode D_{pm} in Figure 2.4. We do not observe any discernible trend in size-distribution with the distance from the source fires in either median diameter or number concentration. This lack of a trend suggests that the microphysical processing during the range of distances sampled has smaller effects on the size distribution than the variability between plumes for Flight b622. Similarly small inter-transect variation was seen for Flight

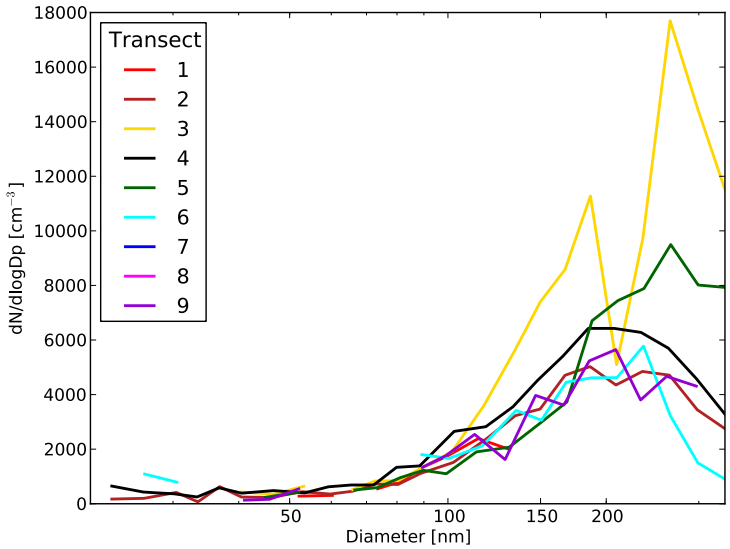

FIGURE 2.3. Median plume number size distributions (corrected to cm^{-3} at STP) divided by transect for Flight b622. All size distributions show a consistent accumulation mode with D_{pm}~220 nm. Size bins with less than three data points in any transect are not shown, limiting the contributions from transects 1, 7 and 8. The composite plume size-distribution for both Flight b622 and b623 is seen in Figure 2.5.

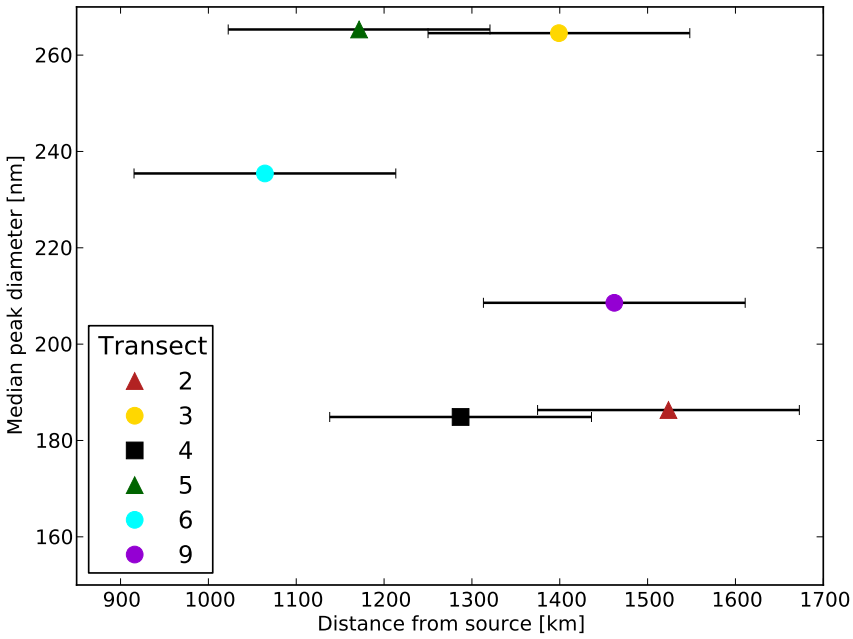

FIGURE 2.4. Accumulation mode peak diameter by transect (2-6, 9) showing no significant trend with plume transport distance for flight b622. All colours are the same as in Figure 2.3. Distance from fire sources was estimated using transect midpoints and approximate source region area. Transects 1, 7 and 8 have insufficient accumulation mode plume data and have been omitted. The uncertainty bars show uncertainty in the distance from the source (± 150 km).

b623. The median size-distributions show no bias based on altitude or ascent/descent rate as an artefact of SMPS flow rate fluctuations from altitude changes (Append. A.4).

Due to the lack of variation between transects, a composite median distribution across all plume sampling periods and both flights is shown in Figure 2.5a. This characteristic size distribution is presented as a median value, minimizing the contributions of outlying data. Figure 2.5b shows the same composite distribution normalized by CO concentration to attempt to account for differences in the amount of emissions from the source. The plume particle size-distribution shows the median size distribution highlighted in black, with the 25th and 75th percentiles outlined in red. A clearly defined accumulation mode was identified centred at D_{pm}= 230 nm and with σ= 1.5, based on a single lognormal mode fit (fit for the entire distribution: D_{pm}= 230 nm, σ= 1.7). Normalizing the plume distribution by CO mixing ratio produced a very similar pattern shown in Figure 2.5b (accumulation mode: D_{pm}= 230 nm, σ= 1.4). The composite background aerosol size-distribution (sampling

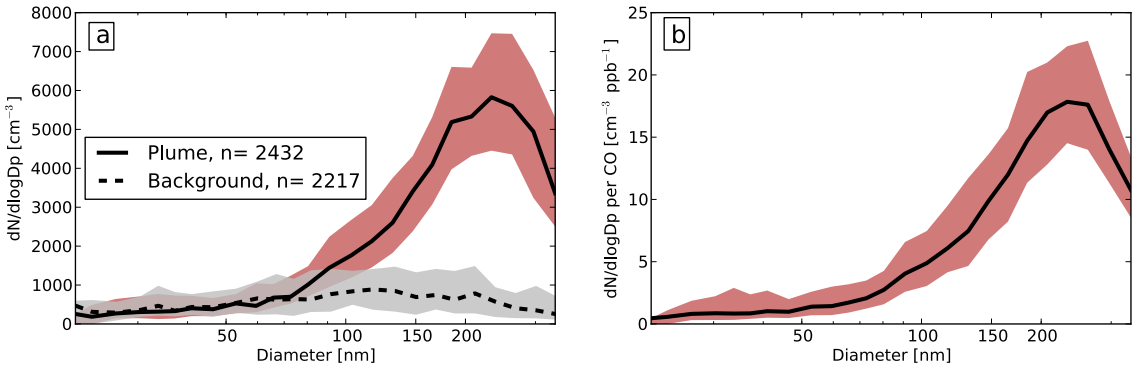

FIGURE 2.5. Composite median number size distributions for Flights b622 and b623 (cm^{-3} at STP). The in-plume (red) and background (grey) air distributions are shown as absolute concentrations (5a). The in-plume distributions are also normalized by CO mixing ratio (5b). The black lines are the median with the 25th and 75th percentiles overlain. The plume distributions have D_{pm}= 230 nm.

periods that failed the in-plume criteria) are seen in black (with 25th and 75th percentiles shown in gray) in Figure 2.5a. It shows relatively constant dN/dlogDp concentrations across the SMPS range and is lacking the concentrated accumulation mode found in-plume.

The aged composite size-distribution and associated lognormal parameters are similar to those found in other field studies of aged biomass-burning emissions. Aged biomass-burning size distributions compiled by Janhäll et al. (2010) for all different fuel types show a similar D_{pm} to modal width ratio (D_{pm}= 175 - 300 nm, σ= 1.7 - 1.3). Capes et al. (2008) show similar aged BB size distribution parameters over West Africa during the DABEX campaign (D_{pm}= 240 nm). The ARCTAS-B campaign over Northern Canada sampled similar Boreal pyrogenic outflow and collected very similar aged distributions of BC and OC constituents (D_{pm}= 224 $\pm$ 14 nm, σ= 1.33 $\pm$ 0.05)(Kondo et al., 2011).

Of note in the BORTAS-B plume size distribution is the elevated number concentrations of small diameter particles (20-90 nm), which form an elevated small-diameter 'tail' of the distribution. These higher concentrations were not expected due to the high rate of removal of small particles by coagulation with the larger particles in the accumulation mode. We calculated first-order coagulational-loss timescales to investigate the timescale of the removal of these small particles by the larger plume particles. If these small particles were brought

into the plume by entrainment of background air, there would be an associated amount of time before these particles were lost by coagulation. For the calculation, we assume brownian coagulation of entrained background aerosol (bin range 20-90 nm) with the observed in-plume SMPS data (90-333 nm) and with artificial large diameter bins from 330 nm - 1 μm (6 bins). These artificial bin concentrations were based on the accumulation mode lognormal fit and account for those particle concentrations at sizes larger than those measured by the SMPS but that nonetheless contribute to the coagulational scavenging of the small-diameter particles. Particles with diameters >1 μm were ignored since their relative scarcity relative to the large number of accumulation-mode particles causes a negligible impact on the number-concentration driven coagulation process.

The predicted concentrations of background aerosol remaining after 24, 36 and 48 hours are shown in Figure 2.6a. These times are within the estimated physical transport age ranges of the transects. After 12 hours, coagulation alone has already caused a significant decrease in the concentrations of the smallest measured particles, reducing them to levels well below the concentrations observed in plume (red line). This deficit increases with time (t=36 hrs, t=48 hrs). The coagulation lifetimes of the particles in this diameter range (30-90 nm) are seen in Figure 2.6b and extend into the tens of hours. Note that the concentrations of these small-diameter particles are similar in the plume compared to the background. This means that the entrainment rate of background air into the plume would need to be much faster than the coagulational loss timescales ($\sim$5 hours for 20 nm particles) in order for entrainment to sustain the number of small particles. If entrainment timescales were significantly shorter than 5 hours, the plume would almost completely disperse into the background within 1 day.

There are a number of mechanisms other than entrainment that could explain the higher tail concentrations found in plume despite the short coagulation lifetimes. In-plume nucleation and subsequent growth to SMPS-detectable sizes could also partially account for sustained elevated small particle concentrations. Hennigan et al. (2012) showed with the FLAME-III chamber studies that in-plume nucleation was possible as a result of photochemical aging and SOA production in smoke plumes. Nucleation modes in association with

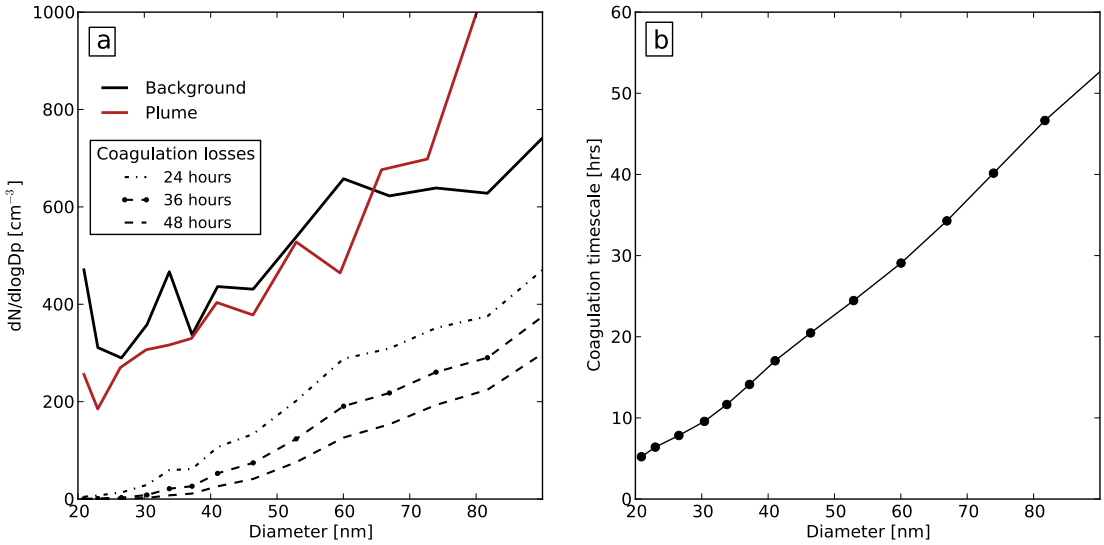

FIGURE 2.6. Figure 2.6a shows background (black solid line) and plume (red line) median concentrations for small particle diameters (20-90 nm). The black dashed lines are the number distributions after 24, 36 and 48 hours of coagulational losses by the plume accumulation mode (Figure 2.5a) from the background level concentrations. These calculated concentrations are much lower than those found in plume. Figure 2.6b shows the coagulation lifetime as a function of particle diameter (on the order of 10s of hours in this diameter range).

smoke plumes have also been observed previously in field studies (Hobbs et al., 2003; Rissler et al., 2006). We attempted to determine the nucleation and growth rates required to sustain the observed concentration of small particles; however, the necessary nucleation and growth rates that we determined were unrealistic, which we see as evidence against nucleation/growth being the primary source of the small particles. Thus, we are unsure of what is the source of these particles.

2.3.2 Net production/loss of organic aerosol with time

Enhancement ratios are a way of characterizing plume chemistry as a ratio of a specific species to a reference species. This was done for the sampled BORTAS pyrogenic outflow by taking the excess (background concentration removed) of the AMS organic aerosol normalized to the excess CO (ΔOA/ΔCO). Only those data which were in excess of the mean background (CO = 100 ppbv, OA = 2 μg m^{-3}) were compiled. The characteristic ΔOA/ΔCO ratio can

be used as a comparison value between fires of different fuel type, phases or photochemical ages.

Since CO has a sufficiently long lifetime and is co-emitted with OA in abundance at the source, any changes in the organic aerosol enhancement ratio over the lifetime of the plume are attributed to in-plume chemistry. The formation of secondary organic aerosol is possible within the plume by oxidation mechanisms to lower volatility products. Some fraction of the semi-volatile SOA can then condense onto the existing condensation sink (Hennigan et al., 2011), increasing the OA fraction detected within the particle. Evaporation of less-volatile POA during plume dilution competes with the SOA condensation. The net OA production is therefore:

$$\Delta OA_{net} = SOA_{prod} - OA_{evap} \tag{2.1}$$

Changes in the ΔOA/ΔCO ratio over time can therefore indicate which of the two processes is dominant.

The organic aerosol enhancement ratios for Flight b622 are shown in Figure 2.7. There is a fairly pronounced altitude dependence as seen in Figure 2.7a, with several high altitude ($\sim$7 km) samples having fairly low excess organic aerosol, but significant ΔCO (300 ppbv). This trend is featured in Franklin et al. (2014) where the high-altitude plume showed evidence of an aerosol rainout event causing low ΔOA/ΔCO within the plume transected at those high altitudes.

We will focus on the lower-altitude plume where the aerosol was not rained out, so we employ a height cutoff of 4.6 km to restrict the enhancement ratio calculations to lower-altitude, OA-rich plumes least likely to have seen significant reduction in organic aerosol from wet deposition. The mean enhancement ratios by transect are seen in Figure 2.7b (for transect locations see Figure 2.1). Only those sampling periods that passed the OA and CO plume criteria (detailed above) are shown. The lower-altitude plume enhancement ratio show correlations of R^2<0.5 for each transect with the exception of Transect 8 (R^2=0.26).

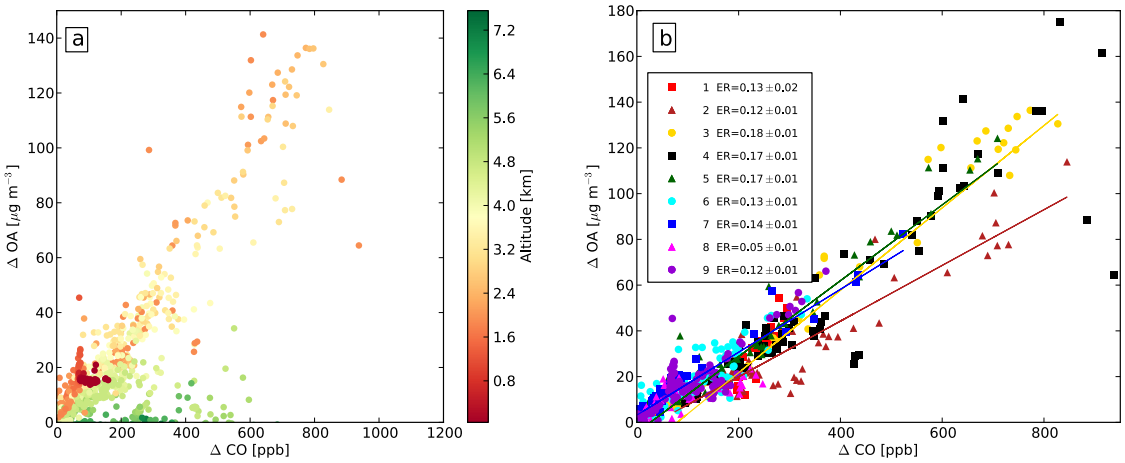

FIGURE 2.7. Enhancement ratios of ΔOA/ΔCO for Flight b622. Figure 2.7a is coloured by altitude showing potential aerosol washout in the high-altitude plume (>4.6 km). Figure 2.7b shows the ERs separated by flight transect showing individual enhancement ratios of between 0.05-0.18 ± 0.01μg m^{-3}ppbv^{-1} with generally high correlation coefficients (R^2>0.7) for the majority. The data points collected at altitudes greater than 4.6 km have been removed (as per 2.7a).

Figure 2.8 shows ΔOA/ΔCO as a function of the distance from the source fires (horizontal error bars correspond to error due to the radius of the Ontario fire region, vertical error bars are calculated from transect data scatter). Compared across transects, the enhancement ratios show no significant trend (to P-value = 0.55). The average enhancement ratio is 0.13 ± 0.01 [μg m^{-3}ppbv^{-1}] and can be considered characteristic of the aged boreal plume during these BORTAS flights.

The lack of trend in Figure 2.8 suggests that we cannot determine if there was any net production/evaporation of OA happening inside the plume. Any SOA produced photochemically inside the plume is either being accompanied by an opposing loss of POA or at such a rate that is below the observational variability over the sampled time period. The statistically invariant ΔOA/ΔCO does not discount evaporation-condensational cycling of POA and SOA, or the effects such recondensation would have on the size-distribution (although there was no apparent trend in the size distribution either [Figure 2.4]). No increase in normalized excess OA fraction means significant levels of excess SOA were not likely driving condensational growth, ensuring that coagulation was dominating the size-distribution evolution

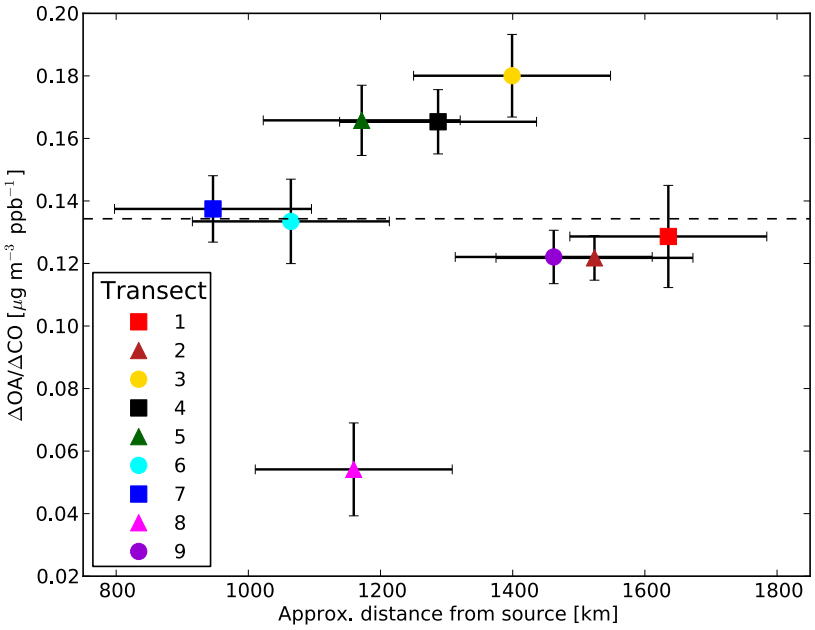

FIGURE 2.8. Transect ΔOA/ΔCO enhancement ratios for Flight b622 as a function of the distance from the source fire region. The average ER is represented by the dashed black line (0.134 μg m^{-3}ppbv^{-1}). There is no discernible trend in ΔOA enhancement either by distance (x-axis) or time (colours). The uncertainty bars display the uncertainty in distance and in fitted enhancement ratios.

during the period of aging between 1 day and 2 days since emission. Since no significant trend was found in size-distribution D_{pm} with distance from the source in the observations (see Figure 2.4), any effect of POA-SOA cycling on the shape of the distribution cannot be isolated above the noise. However, it does not preclude that there was significant net OA production/evaporation that occurred prior to or after this observed period. Thus, although evidence of photo-oxidation and chemical processing was observed in-plume by Parrington et al. (2013), any chemical composition impact on the size-distribution seems negligible.

2.3.3 Estimation of the fresh biomass burning size distribution

In this section, we test the parameter space of our microphysical model to estimate the fresh plume size-distribution emitted from the source fires. We allowed the fresh biomass-burning size distribution to evolve for 48 hours and compared the result to the observed SMPS plume composite distribution to isolate the optimal fresh plume size-distribution parameters. These were then compared to observed fresh BB size distributions for context.

The Lagrangian microphysical model was run for 48 hours with fixed entrainment coefficients of τ_{dil} =24 hrs, τ_{dil} = 36 hours and τ_{dil} =48 hours. Figure 2.9a shows the optimal fresh plume distribution parameters that were obtained for each tested entrainment rate. Figure 2.9b shows the modelled aged distributions plotted with the measured distribution. None of the model runs can capture the elevated concentrations in the tail particles in the SMPS data, though this is expected due to the coagulation-dominant aging in the model (discussed above) and adds further uncertainty to the existence of this small tail.

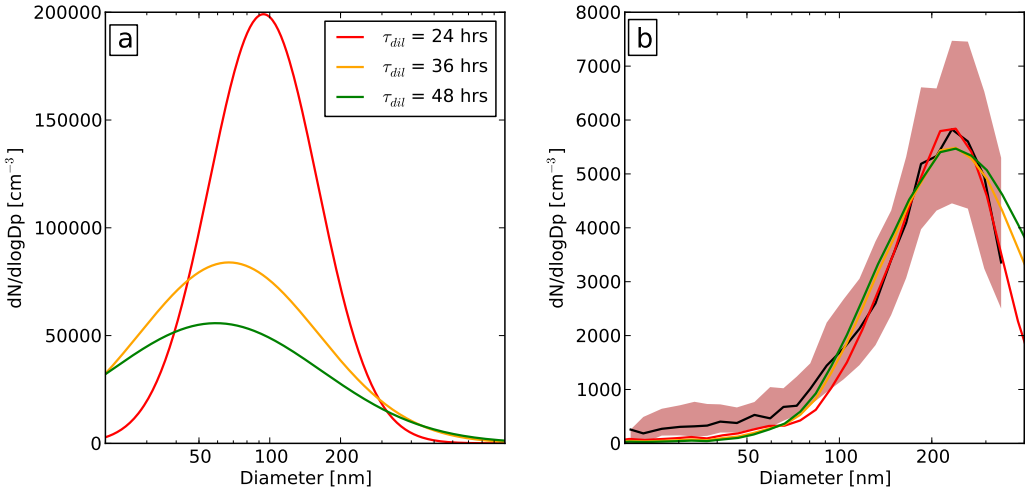

FIGURE 2.9. Figure 2.9a shows the optimized fresh-plume size-distributions for entrainment parameters τ_{dil} = 24, 36, 48 hrs. Figure 2.9b shows the final modelled size-distributions compared to the measured aged plume size-distribution (black median, red quartiles).

The fresh plume size-distributions are unimodal with median diameters of 94 nm, 67 nm, and 59 nm for τ_{dil} =24 hrs, τ_{dil} =36 hrs and τ_{dil} =48 hrs respectively (σ= 1.7, 2.1, 2.8, respectively). The higher entrainment rate of background aerosol requires the fresh plume distribution to be narrower (lower σ) and have an initial median diameter closer to the final diameter (D_{pm}= 230 nm). The initial number concentrations in the fresh plume were found to be optimized at 62,500, 80,000, and 115,000 [cm^{-3}] for τ_{dil} =48 hrs, τ_{dil} =36 hrs and τ_{dil} =24 hrs respectively. The initial higher concentrations, narrower modal width and larger median diameter are required for the higher entrainment rates to account for the more rapid plume dilution and subsequently the slowing of the coagulation rates.

As the exact aging time and dilution profiles are unknown in addition to uncertainties in the plume age, we cannot say with certainty which of these estimates is best; however, these results compare to the field observations presented in Janhäll et al. (2010) for fresh plume smoke (range: D_{pm}= 100-150 nm) and to small-scale lab experiments measuring fresh smoke (range: D_{pm}= 30-90 nm) (Hosseini et al., 2010). Capes et al. (2008) conducted a similar fresh-plume size-distribution estimate from their observed DABEX aged African smoke data using a coagulation box-model without dilution. Their estimates for very fresh smoke have a much smaller D_{pm} (∼30 nm).

The fresh plume size distributions modelled here are very sensitive to microphysical processes directly after emission. Very close to the source, rapid dilution and condensation (due to cooling) may occur, which are not captured by the coagulation/dilution model we have developed. The fresh-plume distributions modelled in this study neglect any immediate effects of condensation and/or evaporation of OA on the size-distribution during cooling and

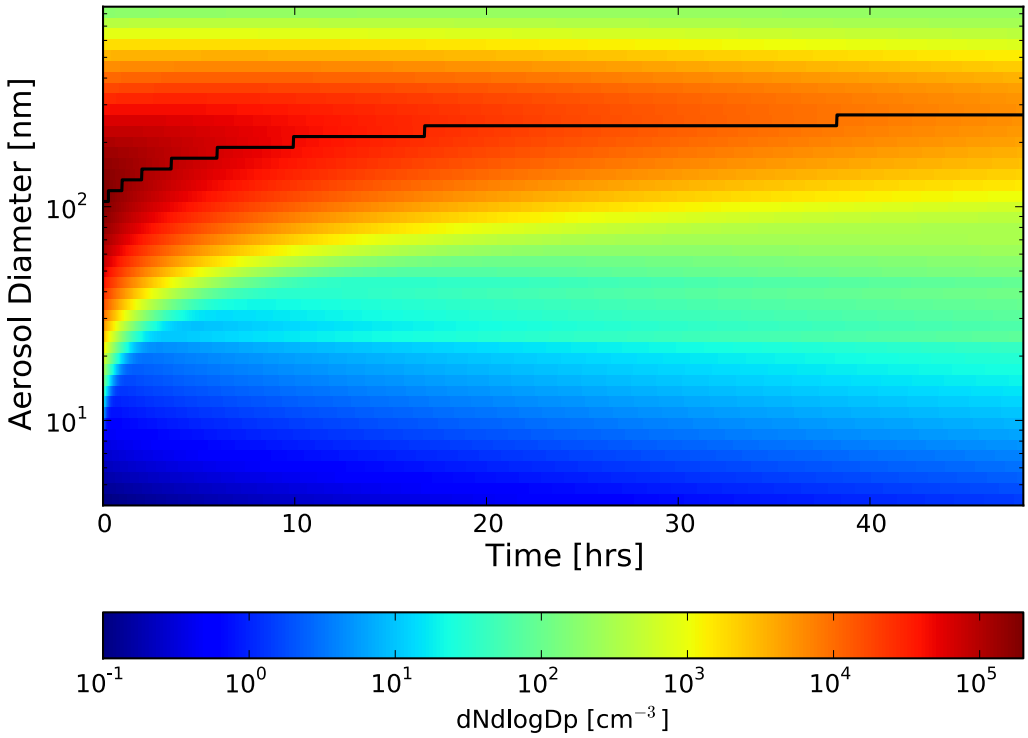

FIGURE 2.10. Plot of modelled size-distribution evolution for τ_{dil} = 36 hrs. The black line shows the peak diameter at each timestep (Δt = 10s). The fresh-plume size-distribution has optimal initial parameters: D_{pm}=67 nm, σ=2.4, N_0 = 80,000 cm^{-3}.

dilution respectively, and focus on the effects of coagulation which shape the size-distribution over a longer timescale (∼10hrs).

Figure 2.10 shows a time series of the optimal modelled size distribution for $\tau_{dil} = 36$ hrs over a 48 hr period. The median diameter growth (black line) occurs more rapidly during the early stages of the plume due to the higher particle concentrations before significant dilution. Eighty percent of the final median diameter is achieved within 10 hrs of coagulation processing. Less drastic but similar rapid growth by coagulation was seen by Capes et al. (2008) in their coagulation box model. This quick size distribution evolution within the early plume stages suggests that large grid box models (global, regional) should be using aged biomass-burning size-distributions as input.

2.4 Conclusions

The BORTAS-B campaign provided the opportunity to collect numerous gaseous and aerosol measurements from aged North-American biomass-burning plumes in July, 2011. The boreal fire emissions in northwestern Ontario were transported (1-2 days) downwind to where they were sampled by the FAAM BAE-146 research aircraft. We analyzed the plume data from two research flights (b622 and b623) and found little variation in size-distributions between transects.

A characteristic size-distribution consistent between flights and transects was dominated by the accumulation mode with D_{pm}= 230 nm and with σ= 1.5. This unimodal result is consistent with aged biomass-burning observations found globally in the previous field studies (Capes et al., 2008; Janhäll et al., 2010; Kondo et al., 2011).

We also found elevated concentrations of small-diameter particles in the plume contrary to their coagulation lifetimes associated with the biomass-burning-associated accumulation mode. We were not able to explain such concentrations by entrainment of background aerosol alone. The presence of such concentrations in the size-distribution tail remains inconclusive.

The ΔOA/ΔCO enhancement ratios across Flight b622 show a strong linear correlation below 4.6 km (8 of 9 transects have R^2 >0.50) with values between (0.05 - 0.18) ± 0.01

μg m^{-3}ppbv^{-1} . We found no trend in transect enhancement ratios with distance from the source, indicating no significant net SOA production in-plume over the sampling period.

We used a microphysical model to estimate the fresh plume size distribution associated with the BORTAS-B observations. Optimizing lognormal parameters for different assumed dilution coefficients (τ_{dil} = 24, 36, 48 hrs), the fresh plume size distribution had D_{pm}= 59-94 nm, σ= 2.8-1.7, and N_0 = 62,500 -115,000 cm^{-3}. Though the model lacks condensation and chemical considerations, processing through coagulation and dilution alone led to 80% of the observed 48-hour median-diameter growth within the first 10 hrs. This suggests that global climate models should be using coagulation-aged BB size distribution inputs to account for the rapid evolution in plume particle size occurring on scales smaller than the gridbox length.

3. The evolution of biomass-burning aerosol size distributions: High-resolution modelling and parameterization for regional and global aerosol models[3]

3.1 Objectives

In this chapter, we investigate the factors that shape aged biomass burning (BB) size distribution for cases where there is no organic aerosol production or loss. These factors include fire area, aerosol emissions flux, emissions size, and meteorological conditions. We create a parameterization of D_{pm} (dry median particle diameter) and σ (modal width) of the aged biomass-burning size-distributions, as a function of these input parameters based on simulations from a large-eddy model with embedded aerosol microphysics (SAM-TOMAS). Accurate representation of aged BB aerosol size is necessary for accurate CCN predictions in coarse regional and global models (Lee et al., 2013; Pierce and Adams, 2009; Spracklen et al., 2011). This need for aged BB size-distributions necessitates understanding aerosol size-distribution processing that occurs within concentrated sub-grid-sized plumes. While we do not explicitly simulate the production or loss of organic aerosol we provide corrections for our parameterization for cases where production/loss rates are known. This production/loss of organic aerosol has considerable uncertainty, and we will argue that variability in other factors likely leads to more variability in the aged size distribution than OA production and loss.

An overview of the parameterization building process, including the use of a Gaussian emulator, is provided in Section 3.2.1. A discussion of input and output ranges, processing, and constraints of the parameters we study is provided in Section 3.2.2. The SAM-TOMAS model and the emulation process are discussed in Sections 3.2.3-3.2.4. The SAM-TOMAS size-distribution results are presented in Section 3.3.1. A comparison between the emulator and the SAM-TOMAS model is found in Section 3.3.2. The emulator sensitivities to the inputs are discussed in Section 3.3.3. Simplified fit equations for D_{pm} and σ are shown in

[3]Chapter 3 in prep. for: Sakamoto, K. M., Stevens, R. G. And Pierce, J. R.: The evolution of biomass-burning aerosol size distributions in the absence of organic aerosol condensation/evaporation. Atmos. Chem. Phys.

Section 3.3.4, with a discussion of potential OA production/loss effects in Section 3.3.5. We conclude in Section 3.4, including future plans for testing the parameterization and known existing limitations.

3.2 Experimental Methods

3.2.1 Overview of methods

The parameterization was built according to the process depicted in Figure 3.1. The process involves a Large-Eddy simulation model, the System for Atmospheric Modelling (SAM, Khairoutdinov and Randall (2003)), with the online aerosol microphysics module, TwO Moment Aerosol Sectional (TOMAS, Adams and Seinfeld (2002); Stevens et al. (2012)), for 100 training cases that span a range of input parameters relevant to the coagulational aging of biomass-burning aerosol. These cases are used to build a statistical emulator (in our study, by using the Gaussian Emulation Machine for Sensitivity Analysis, GEM-SA) to

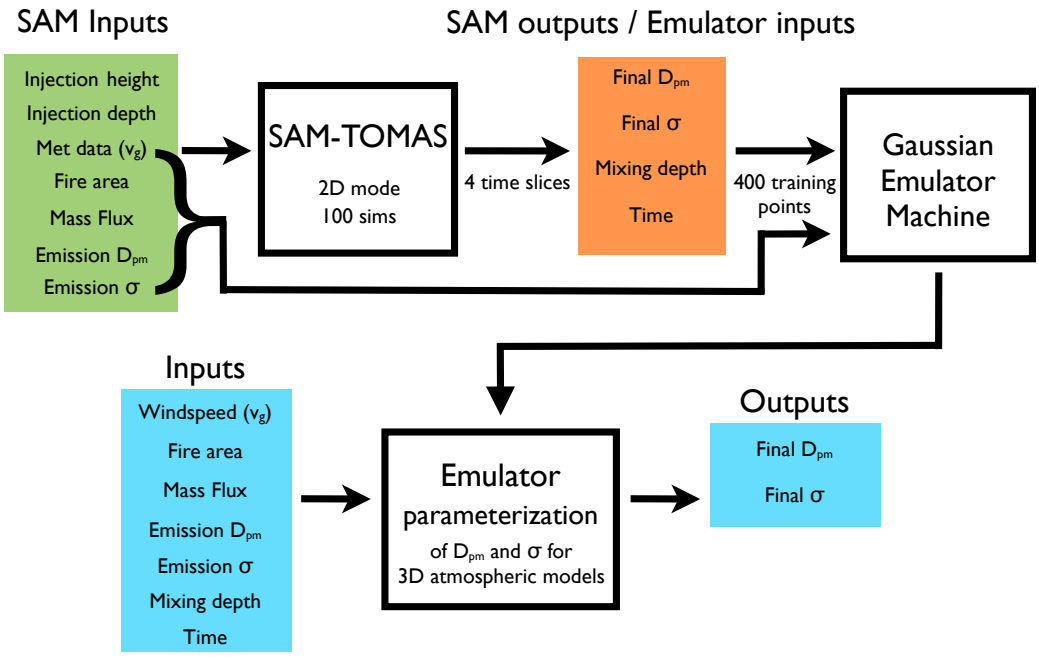

FIGURE 3.1. Abstract schematic of the parameterization-building process. SAM-TOMAS simulation outputs are used as inputs to the Gaussian Emulation Machine for Sensitivity Analysis (GEM-SA). The emulator parameterization is used to predict D_{pm} and σ based on 7 inputs: windspeed (v_g), fire area, mass emission flux, emission D_{pm_0}, emission σ_0, mixing depth, and time.

replace the full model in order to make testing the parameter space more computationally efficient. This approach is advantageous because only a small number of full SAM-TOMAS runs (in this case, 100) are required to train the emulator across a 7-input-parameter space. This technique was previously employed by Lee et al. (2011) in an investigation of CCN uncertainties in the global chemical transport model, GLOMAP (Lee et al., 2012, 2013).

We performed 100 SAM-TOMAS model simulations while varying 7 input parameters between simulations: emission D_{pm_0}, emission σ_0, emission mass flux, fire area, meteorology (includes average boundary layer windspeed, v_g), emission injection height, and emission injection depth (described further in Sect. 3.2.2, see Table 3.2). The output from SAM-TOMAS was recorded at four different times (400 time slices across 100 simulations). For each time slice, the D_{pm} and σ of the size-distributions at that time were calculated, in addition to the aerosol plume mixing depth (d_{mixing}).

These three SAM-TOMAS outputs, along with a subset of the initial parameters, undergo criteria filtering (see Sect. 3.2.2) and become the GEM-SA emulator training data (maximum of 400 training points). The GEM-SA program then generates an emulator of both D_{pm} and σ as functions of 7 input parameters (see Table 3.1). The emulator requires 7 input parameters: emission D_{pm_0}, emission σ_0, mass flux, fire area, windspeed (v_g), mixing depth (d_{mixing}) and time, and generates predicted final D_{pm} and σ as outputs for use as effective lognormal BB size-distributions. The behavior of the emulator can then be tested across a range of realistic input-parameter values. The advantage of this setup is that while SAM-TOMAS simulations are computationally expensive, the emulator is comparatively cheap, so we may use the emulator to increase the number of simulations to well beyond the 100 SAM-TOMAS cases. Finally, we provide simplified, single-equation approximations for D_{pm} and σ that may be more convenient for regional/global model use than the full emulator created by GEM-SA.

3.2.2 *Investigated factors that may lead to variability in aged size distributions*

Based on field and lab observations of fresh and aged BB aerosol (Levin et al., 2010; Sakamoto et al., 2014; Janhäll et al., 2010; Capes et al., 2008), a single lognormal mode specified by D_{pm} and σ is believed to be sufficient for BB aerosol representation. Both the SAM-TOMAS model and the final parameterization will therefore have a single BB aerosol mode to represent the initial and final size distributions. Similar single-mode size-distribution evolution by coagulation has previously been modelled in ship track plumes (Stuart et al., 2013) and background aerosol (Stevens and Pierce, 2013; Pierce and Adams, 2009; Stevens and Pierce, 2014).

An effective parameterization needs to accurately represent BB size-distribution aging using inputs that are generally available in large-scale aerosol models. The seven parameters chosen as inputs to the parameterization can be divided into those representing the initial size-distributions (D_{pm_0}, σ_0), fire conditions (mass flux, fire area), atmospheric conditions (v_g, d_{mixing}), and time. All are potentially important factors in coagulational plume processing. A summary of the input parameters and appropriate ranges of our parameterization are found in Table 3.1.

The initial size-distribution parameters specify the median diameter (D_{pm_0}) and modal width (σ_0) of the freshly emitted aerosol distribution. For the parameterization they were varied between 20–100 nm in D_{pm_0} and 1.2-2.4 in σ_0. The large ranges are due to combustion,

TABLE 3.1. Parameter ranges for each of the 7 inputs to the parameterization.

Parameter	*Description*	*Units*	*Min. value*	*Max. value*
D_{pm_0}	Emission median dry diameter	nm	20	100
σ_0	Emission modal width	–	1.2	2.4
Mass flux	Emission mass flux from fire	kg m^{-2} s^{-1}	2×10^{-8}	5×10^{-6}
Fire area	Square fire emissions area	km^2	1	49
v_g	Windspeed	ms^{-1}	2	20
d_{mixing}	Mixing depth of aerosol layer	m	150	2500
Time	Time since emission	min	0	300

time and fuel-type factors as seen in lab and observational studies (Levin et al., 2010; Janhäll et al., 2010), and our modelled fresh size-distributions from BORTAS-B (Section 2.3). We expect coagulational growth of D_{pm} to larger sizes regardless of D_{pm_0}, but σ convergence to the Brownian-coagulational limit of ∼1.32 found by Lee (1983) as the plume ages.

Fire area, mass flux, and windspeed all effect the number and mass aerosol concentration within the plume, which in turn affects the coagulation rate ($J_{coag} \propto N^2$). Large mass fluxes over larger fire areas result in higher emitted aerosol mass per second. Large fire areas are less susceptible to plume dilution by entrainment of background air. Combined with slower boundary layer windspeeds, this results in more concentrated plumes (higher N), faster coagulation and faster size-distribution shifts. In this study, emissions mass flux was constrained to 2×10^{-8} – 5×10^{-6} kg m^{-2} s^{-1} using approximate maximum and minimum values of summed black carbon and organic carbon flux (BC+OC) found in the Global Fire Emissions Database ver. 3 (GFED3). Fire area ranged from 1 - 49 km^2 (simulated as a square), which was found to represent the range of fire sizes in GFED3. Boundary layer windspeed, v_g, varied between 2 m s^{-1} and 20 m s^{-1} and was based on NCEP reanalysis meteorology.

Mixing depth (d_{mixing}) is defined as the vertical extent of the aerosol plume at a given time. All other factors being equal, aerosol plumes mixed through larger depths are more dilute than those concentrated in thinner layers. This dilution leads to a lowering of plume aerosol concentration (lower N) and slower coagulation rates. Mixing depth had a range over 150–2500 m (based on SAM-TOMAS output). Time is the final input parameter and we expect coagulation to slow with time as N decreases. Five hours (300 min) was chosen as an upper time bound due to this effect and the large associated distance from the source fire.

3.2.3 The SAM-TOMAS model

The model used in this investigation was the System for Atmospheric Modelling (SAM; Khairoutdinov and Randall (2003)), a dynamical large-eddy simulation (LES). SAM is capable of <1 km resolution and ∼100 km domain, making it ideal for use as a regional plume

model. The model can be run in 2D mode, in which a wall oriented normal to the mean boundary layer wind and moving at the mean boundary-layer wind speed v_g is used to track the plume evolution downwind as seen in Figure 3.2. This 2D mode is computationally efficient compared to the full 3D model with very minor differences due to axial plume symmetry (Stevens and Pierce, 2013).

The size-distributions of the aerosol particles were processed using the TwO Moment Aerosol Sectional (TOMAS; Adams and Seinfeld (2002)) microphysical scheme embedded into SAM. The algorithm simulates the BB size-distribution across 15 logarithmically-spaced size bins spanning 3 nm–10 μm. The aerosol size distribution is tracked via two independent moments for each bin of the size-distribution (mass and number). It calculates coagulation explicitly in each grid-cell assuming a Brownian diffusion kernel. This means the coagulation rate (J) between any two bins can be expressed as:

$$J_{ij} = K_{ij} N_i N_j$$

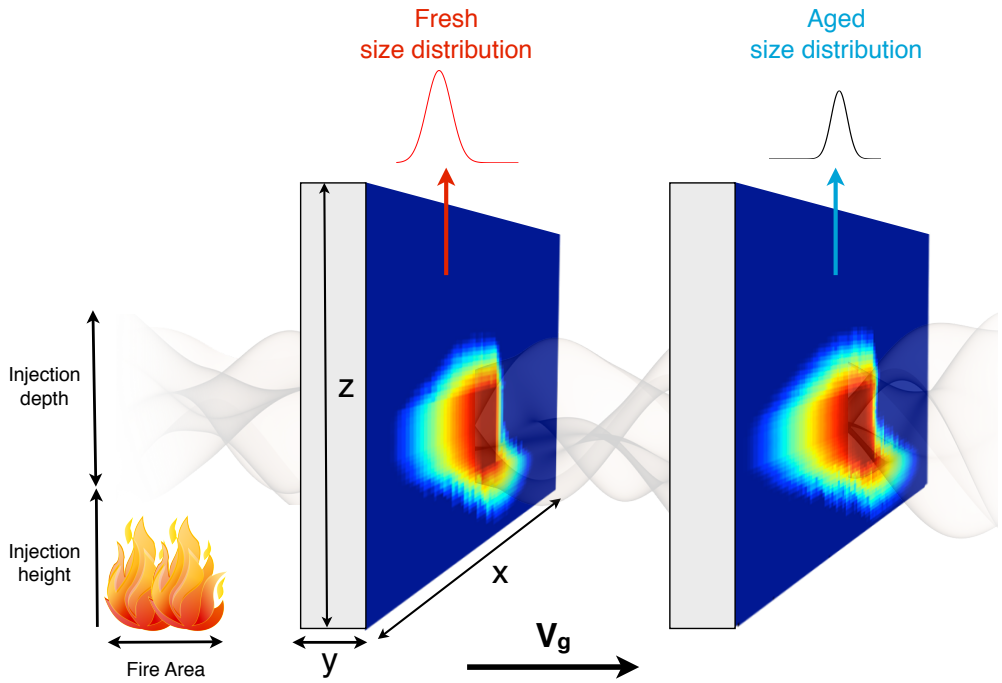

FIGURE 3.2. Schematic of a 2D SAM-TOMAS plume run. A wall oriented normal to the mean boundary layer wind and moving at speed v_g is used to track the evolution of the plume. The BB plume is defined in part by the fire area, aerosol injection height and aerosol injection depth.

where K_{ij} is the Fuchs coagulation coefficient (Fuchs (1964) Append. A.3) and N_i is the number concentration in bin i. The SAM-TOMAS model has previously been tested against observations in Stevens et al. (2012) and Lonsdale et al. (2012) for power plant plumes.

During this study, SAM-TOMAS was run at a 500 m × 500 m horizontal resolution (100 km domain), and a constant 40 m vertical resolution (vertical extent = 4 km). This resolution accommodated the chosen plume parameters (see Section 3.2.1). TOMAS simulated coagulation with no condensation/evaporation or nucleation. It processed emitted particles of a single-species only (no gaseous products or differentiating between BC and OA). The model was run with a maximum timestep of 2 seconds (varied internally for accuracy in the coagulation calculation) for a duration of 5 model hours (300 minutes).

The seven inputs to the SAM-TOMAS model were constrained to capture a range of biomass-burning characteristics in realistic scenarios and are summarized in Table 3.2. The meteorology fields were supplied by NCEP reanalysis meteorology from over North America (land only, lat: 30° – 70° N, lon: 70°–135° W) during fire season (July, 2010). The SAM-TOMAS wall speed, v_g, was set equal to the mean boundary layer windspeed from NCEP. These inputs were filtered by requiring v_g >2 m s^{-1} to eliminate stagnation situations over the source.

The ranges of values used for D_{pm_0}, σ_0, fire-area and mass flux are the same as those listed in Table 3.1. The injection height (lower bound) and injection depth of the aerosol

TABLE 3.2. Parameter ranges for inputs to the SAM-TOMAS model.

Parameter	*Description*	*Units*	*Min. value*	*Max. value*
Date	Req. for Met. field selection	8-hour	July 1, 2010	July 31, 2010
Latitude		°N	30	70
Longitude		°W	70	135
D_{pm_0}	Emission median dry diameter	nm	20	100
σ_0	Emission modal width	–	1.2	2.4
Mass flux	Emission mass flux from fire	kg m^{-2} s^{-1}	2×10^{-8}	5×10^{-6}
Fire area	Square fire emissions area	km^2	1	49
Injection height	Lower plume injection bound	m	50	150
Injection depth	Depth of plume at emission	m	500	2000

were specified at between 50–1500 m and 500–2000 m respectively. No emission injection parameterization (e.g. Freitas et al. (2007)) was used as we are only trying to capture a range of mixing depths for our aging calculation and the absolute height matters less. All the SAM-TOMAS simulation inputs were chosen using semi-random Latin hypercube sampling across the ranges listed above (Lee et al., 2012).

In the SAM-TOMAS simulations, we set background aerosol concentrations to zero. The BB aerosol concentrations emitted into SAM-TOMAS are orders of magnitude larger than those present in a remote background location, and as such the lack of background aerosol should have an insignificant effect on the rate of in-plume coagulational processing. The BB aerosol was assumed to have a constant density of 1400 kg m^{-3} as primarily a mix of organic compounds, thus we do not consider how changes in BC/OA composition may affect density and coagulation rates. The hygroscopicity of the BB aerosol particles was set to zero, allowing no water uptake (all particle diameters in this study refer to dry diameters). This assumption is not true of real world BB aerosol and has been characterized in other works finding hygroscopicities of fresh (κ=0.02–0.8; Petters et al. (2009)) and aged smoke (κ=0.1–0.3; Engelhart et al. (2012)) with a strong dependence on fuel type. In terms of their effect on the size-distribution however, a constant κ across all particle sizes has the simple effect of increasing the effective diameter of the particles via water uptake by a scalar factor. This initial increase should only have a relatively minor effect on the final dry D_{pm} or σ of the plume after coagulational processing as the mean coagulation rates are relatively insensitive to the size shifting of a particle population (Seinfeld and Pandis, 2006; Stuart et al., 2013).

The mixing depth of the plume (d_{mixing}) was calculated from vertical profiles averaged horizontally across the entire wall. A sample of 6 vertical profiles from different SAM-TOMAS simulations is seen in Figure 3.3. The mixing depth ([m]) was defined as the range of altitudes where the aerosol mass was greater than half of the peak aerosol mass:

$$d_{mixing} = \Delta_{alt} 50\% \text{peak aerosol mass}$$

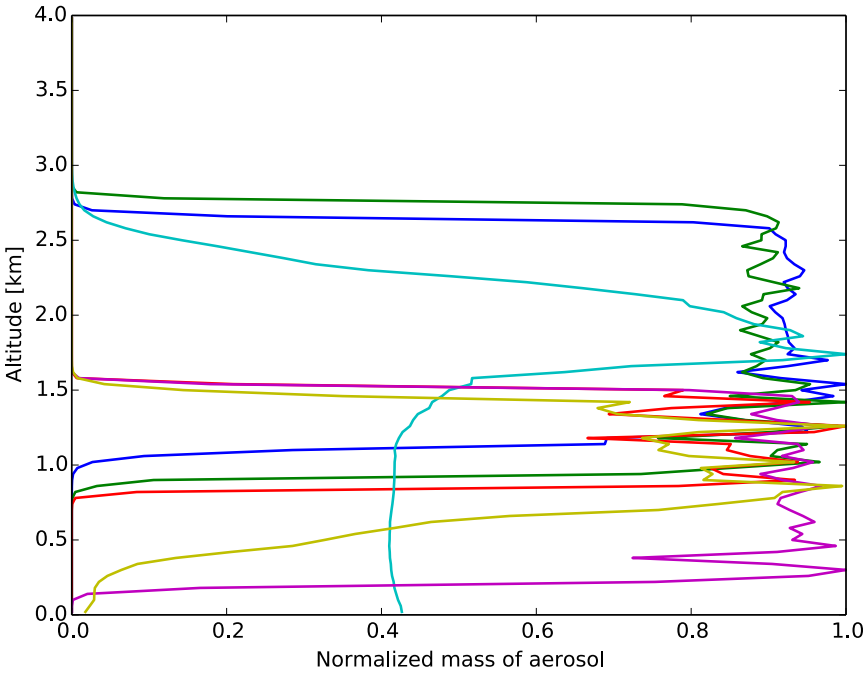

FIGURE 3.3. Final average vertical profiles for 6 SAM-TOMAS simulations after 4 hours, normalized to individual aerosol load. The profiles show a variety of mixing depths, with some fully mixing through the boundary layer, while others are still stable at the emission injection layer.

This was a well-defined quantity for all the SAM-TOMAS runs. In cases where the plume mixed down to the ground, the lower altitude bound was defined as 0 m. Mixing depths greater than 2500 m were excluded from the training data to ensure that the plume did not reach the model top. The final D_{pm} and final σ were calculated for each of the SAM-TOMAS time slices from the first and third moments of the size distribution as detailed by Whitby et al. (1991) (Append. B.1).

3.2.4 Emulation of the SAM-TOMAS output

We used the GEM-SA software to build a statistical approximation of the SAM-TOMAS model (the emulator). The use of an emulator allows us to probe the parameter space rigorously without running the SAM-TOMAS model for each point. We used the Gaussian Emulation Machine for Sensitivity Analysis (GEM-SA) developed by the Centre for Terrestrial Dynamics (http://www.ctcd.group.shef.ac.uk/gem.html). This software was previously

used in sensitivity studies in atmospheric-aerosol (Lee et al., 2011, 2012) and vegetation models (Kennedy et al., 2008).

The GEM-SA software uses a Gaussian process to build a SAM-TOMAS simulator (the emulator) based on the behaviour of the known SAM-TOMAS inputs/outputs (the training data). It assumes parameter smoothness to statistically emulate the model in 7-parameter space (the 7 input parameters to the parameterization) and estimate the model output. A complete description of GEM-SA statistics and assumptions can be found in Kennedy and O'Hagan (2001); Kennedy et al. (2008) and its application as an estimator in atmospheric-aerosol modelling in Lee et al. (2011).The validated emulator was used to generate individual D_{pm} and σ estimated outputs and is run offline via Fortran90 code (Append. B.2).

3.3 Results

3.3.1 SAM-TOMAS simulation output

The influence of several factors (the distance from the source, the mass flux, and the area) on the final aerosol size distributions is apparent in the output of SAM-TOMAS simulations. Figure 3.4 panels a and c show the D_{pm} change as a function of distance for each of the 100 SAM-TOMAS simulations, and panels b and d show the σ change as a function of distance for the same simulations. Panels a and b are colored by the emissions mass flux, whereas panels c and d are colored by dM/dx (kg m^{-1}, the amount of aerosol mass in an infinitesimally thin slice of air perpendicular to v_g, i.e. Mass flux $\times$ Fire area / v_g). All simulations showed D_{pm} increasing with distance as coagulation progressed in each plume. The coloring in panel a shows that D_{pm} generally increases more rapidly and to higher values with higher emissions fluxes. However, panel c shows that dM/dx is a better predictor for the increase of D_{pm} with distance than the emissions flux, and the distance and dM/dx capture much of the variability in D_{pm}. The initial emissions diameter appears to have little influence on D_{pm} (note, however, that the first points on these plots already include some processing and are not the initial diameters).

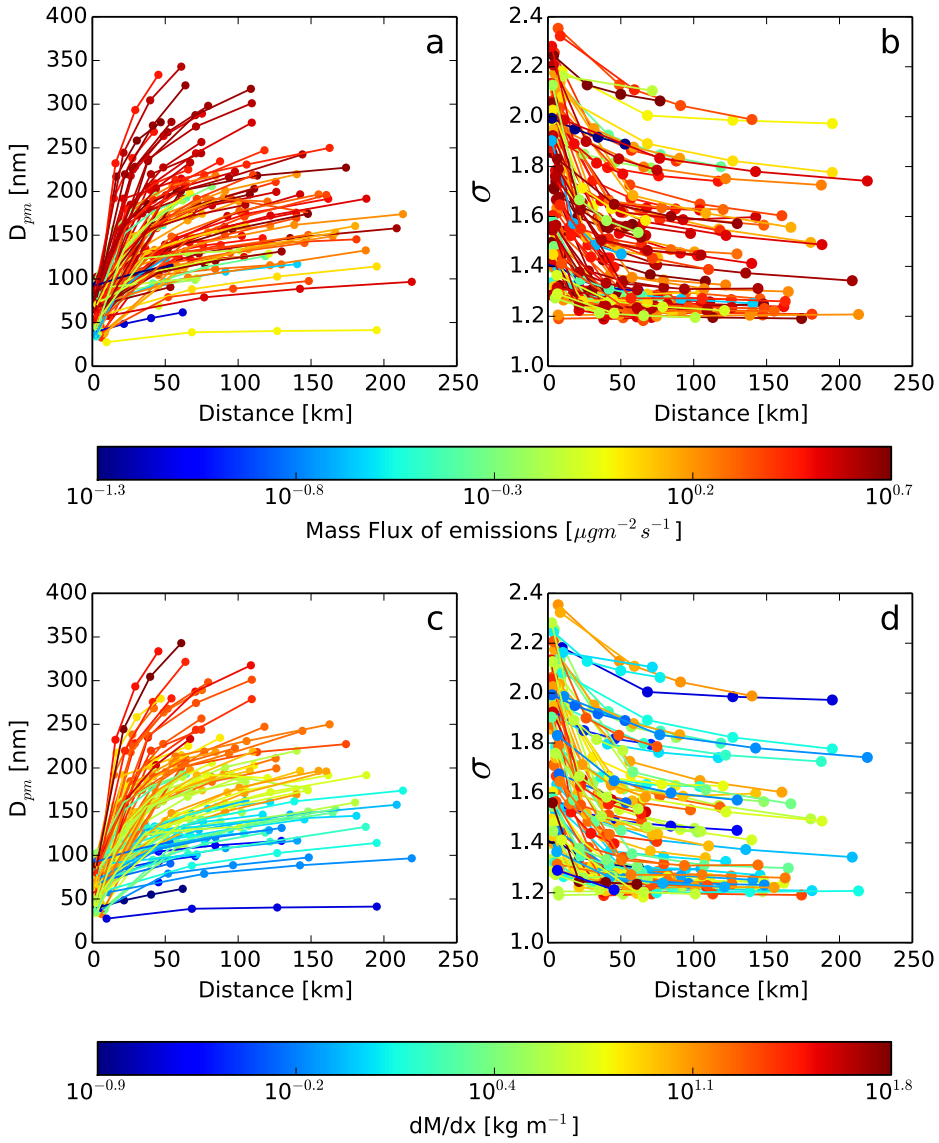

FIGURE 3.4. Wire plots showing size-distribution changes across individual SAM-TOMAS simulations coloured by emission mass flux (3.3a-3.3b) and dM/dx (3.3c-3.3d) for D_{pm} and σ.

Panels b and d show that σ tends to converge with distance with large initial σs decreasing with distance. This convergence happens slowly relative to the times simulated, so the initial σs have a strong influence even at 200 km. The colors and panels b and d show that σs in high emissions-flux and dM/dx cases converge more rapidly than low-emissions cases.. However, as opposed to the 1.32 modal width asymptote found by Lee (1983), the SAM-TOMAS simulations converge to a limit of 1.2-1.25. This is likely due to the size-distribution bin-spacing in the SAM-TOMAS model, where modal widths <1.32 are significantly smaller

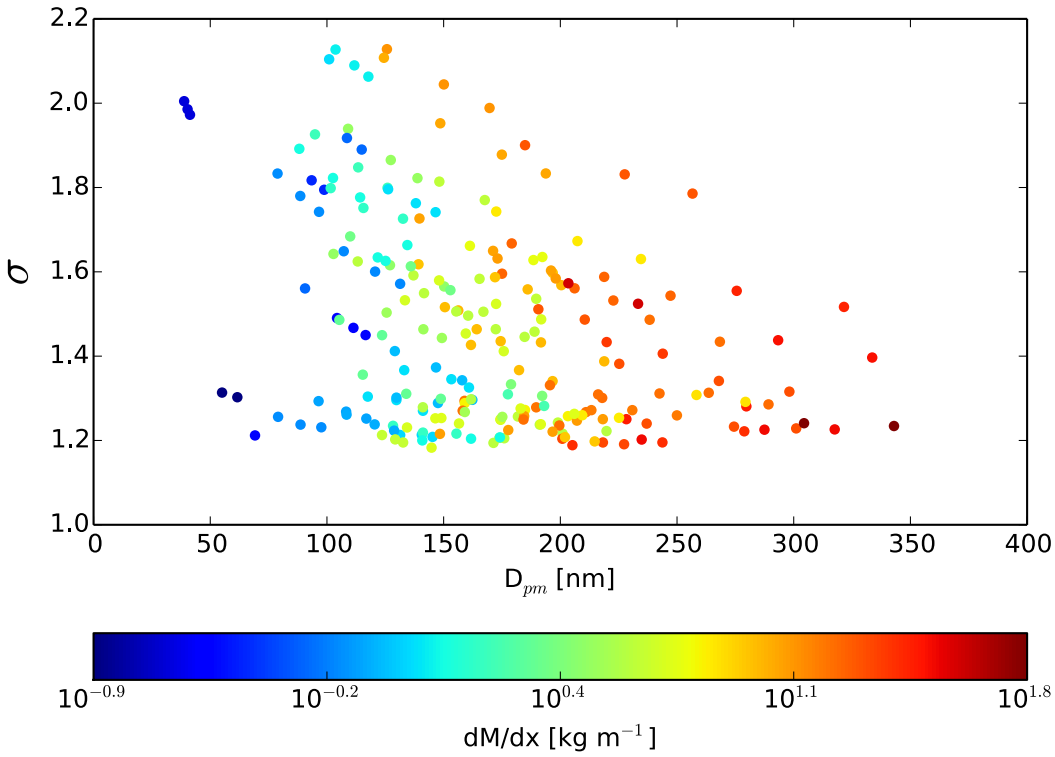

FIGURE 3.5. Scatter plot showing the relationships between final modal width (σ), final D_{pm}, and dM/dx (total mass of emissions normalized to SAM x-gridbox) for each of the 400 simulation slices. The data are filtered for distances >25 km to minimize the influence of the initial size-distribution parameters.

than a single TOMAS size bin width. This mismatch results in less accurate fits of σ as σ decreases and may lead to the covergences towards σ= 1.2-1.25.

Figure 3.5 is a scatterplot of D_{pm} vs σ for each point seen in Figure 3.4, excepting those at distances less than 25 km (initial distances removed). The points are colored by dM/dx. Thus, Figure 3.5 places the results of Figure 3.4b and 3.4d together but removes the distance information. At these distances over 25 km, D_{pm} is relatively well constrained by dM/dx alone, showing that the mean growth by coagulation is strongly influenced by the mass of particles in the slice of air. On the other hand σ is unconstrained at low values of dM/dx but more constrained towards 1.2-1.4 at high values of dM/dx. At high dM/dx values, the convergence towards the steady-state σ proceeds much more rapidly than at low dM/dx as also shown in Figure 3.4d. We use the emulator to determine the effects of the other input parameters on the aged BB size distribution.

These results show that dM/dx (Mass flux × Fire area / v_g) is a powerful determinant of aged biomass burning size. In these tests, we also explored dividing dM/dx by the final mixing depth to create dM/dxdz (Mass flux × Fire area / v_g / mixing depth). Large mixing depths dilute particle concentrations and reduce coagulation, so we expected that dM/dxdz may be a better predictor of biomass burning size-distribution aging than dM/dx. However, Figures 3.4 and 3.5 did not look substantially different when using dM/dxdz (Append. B.3, B.4). We quantitatively evaluate the fidelity of dM/dx and dM/dxdz as proxies for biomass burning size-distribution aging in Section 3.3.4.

3.3.2 Model parameterization evaluation

The GEM-SA–derived emulator parameterization was tested against actual SAM-TOMAS model runs with the results plotted in Figure 3.6. 624 additional SAM-TOMAS–simulated data points that were not used for GEM-SA training are used in this evaluation. The emulator parameterization-predicted outputs corresponding to these data points for D_{pm} and σ are plotted against the SAM-TOMAS D_{pm} and σ . Predicted D_{pm} has an R^2 value of 0.83 with a slope of 0.92. Larger absolute errors in D_{pm} are found at the larger diameter sizes, but 86% are found within 10% of the SAM-TOMAS D_{pm} (76% of predicted D_{pm} are within 5% of actual D_{pm}). The small mean normalized bias (MNB; Append. B.5) of -0.06 indicates a slight negative bias in the parameterization. This is generally seen towards the higher final D_{pm} values in the simulations (>250 nm), which are reached only by the most aged plumes with the heaviest aerosol loads. The σ one-to-one plot shows a similarly high correlation coefficient (R^2=0.91) and has a slope of 0.93. The MNB is very small at 0.01. 77% of the predicted σ points are within 5% of the σ calculated from SAM-TOMAS. The cluster of points near σ=1.2–1.3 is indicative of the modal width steady-state limit. This limit does not seem to be captured by the σ parameterization which assumes a smooth function towards even lower σ values.

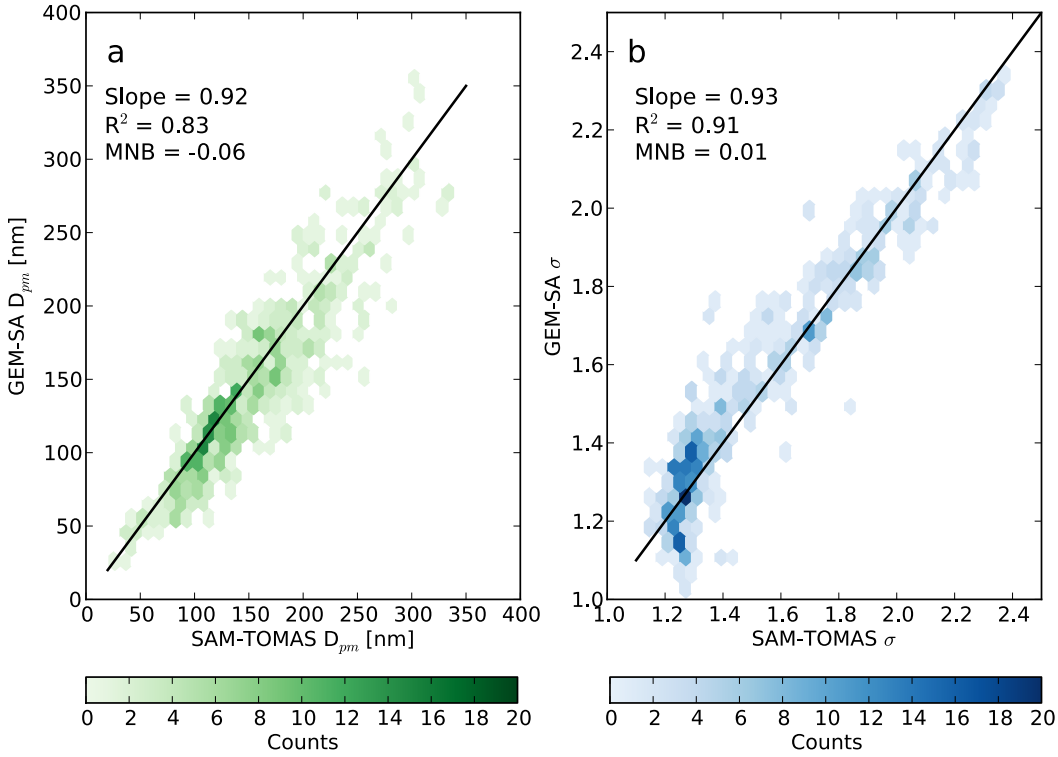

FIGURE 3.6. One-to-one plot showing SAM-TOMAS vs GEM-SA emulator for 624 non-training simulation slices for a) final D_{pm}, and b) final modal width, σ. The black line is the one-to-one line.

3.3.3 GEM-SA sensitivities

Figures 3.7 and 3.8 show the sensitivities of the parameterization outputs (D_{pm} and σ, respectively) to the input parameters (D_{pm_0}, σ_0, mass flux, fire area, v_g, time, and d_{mixing}) as determined by the GEM-SA emulation of the SAM-TOMAS output. In each panel, each line represents the change in D_{pm} (Figure 3.7) or σ (Figure 3.8), $\Delta\%_{output}$, as a parameter (e.g. D_{pm_0} in panel a) is varied systematically from its minimum to maximum value with a randomly chosen set of the other six input parameters. Each panel contains 100 lines, which means that 100 sets of the six other input parameters were randomly chosen to make these lines. The change in $\Delta\%_{output}$ is shown as percentage difference from an input parameter midpoint (time output variance is shown as the percentage difference from t=0 min). The sensitivity plots are meant to show the parameterization's output response to each isolated input variable.

The D_{pm} sensitivity plots (Figure 3.7) show a number of well-defined responses of D_{pm} to the inputs. D_{pm} increases monotonically with increases in mass flux and fire area (Figures 3.5b,d), and decreases nearly monotonically with wind speed, v_g. These trends are due to the interrelationships of these inputs with starting number concentration, N. As dM/dx is Mass flux $\times$ Fire area/ v_g, these results are consistent with Figures 3.4 and 3.5. Additionally, the D_{pm} also decreases monotonically with mixing depth, which leads us to believe that dM/dxdz may also be a good proxy for biomass burning size-distribution aging (evaluated in Section 3.3.4). Higher dM/dx and dM/dxdz values lead to higher initial number concentration in these plumes, which drive higher rates of coagulation due to $J_{coag} \propto N^2$.

Median diameter also increases nearly monotonically with distance (the regions of slight decreases with distance show that the parameterization is not necessarily always physically representative due to the statistical nature of the fit over the parameter space). The very rapid rise in D_{pm} for time <2 hrs is due to the high number concentrations (N) and coagulation rates near the source. As dilution and coagulation progress, N decreases and coagulation slows, resulting in a slowing of D_{pm} increase. Mass flux has the largest range of output D_{pm} associated with the input range specified here ($\sim$100–150% range).

The relationships between D_{pm} and D_{pm_0} and σ_0 is more complicated. Neither Figure 3.4a nor Figure 3.4c show monotonic increases or decreases in D_{pm} due to changes in either of these isolated inputs. This lack of monotonic trend indicates the influence of other factors. In general there is an increasing trend in output D_{pm} with increasing D_{pm_0}, but for some cases it decreases. These decreases in D_{pm} are likely due to decreases in particle number concentrations, due in turn to increases in diameter, which lead to reduced coagulation rates, as well as imperfections in the statistical fit of the parameter space. The larger σ_0 indicate broader emission size-distributions, with more large particles and small particles. Since coagulation progresses fastest between large and small particles (as opposed to particles of approximately the same size), this favors higher D_{pm} at higher σ. However, the initial particle number decreases with increasing σ, which lowers the coagulation rate and leads to lower D_{pm}.

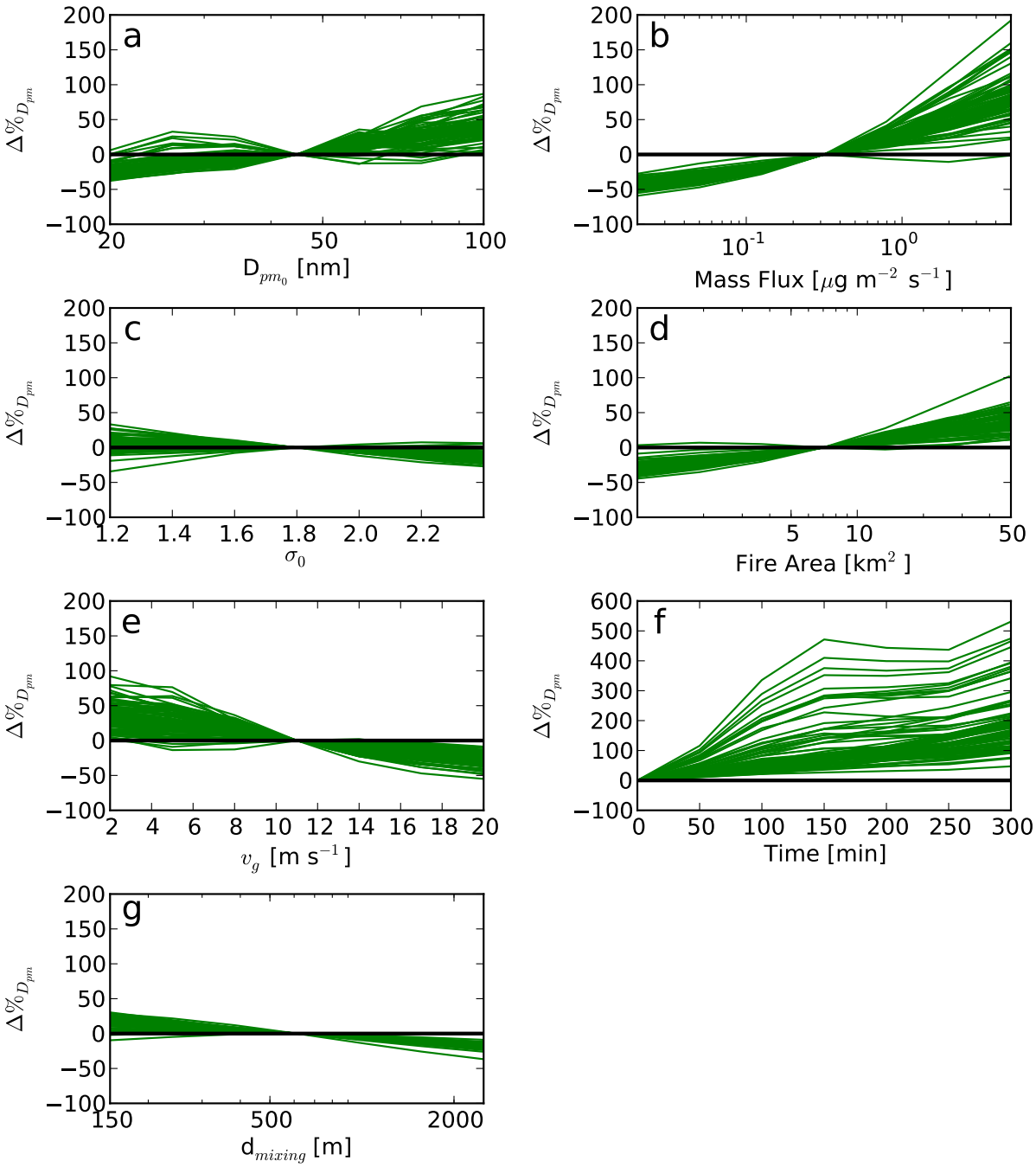

FIGURE 3.7. Sensitivity plots for the 7 input parameters to the GEM-SA D_{pm} parameterization. One hundred random input sets (non-training data) were used. The sensitivities are shown as percent change in final D_{pm}, individually normalized to the center value of the x-axis (to zero in Time).

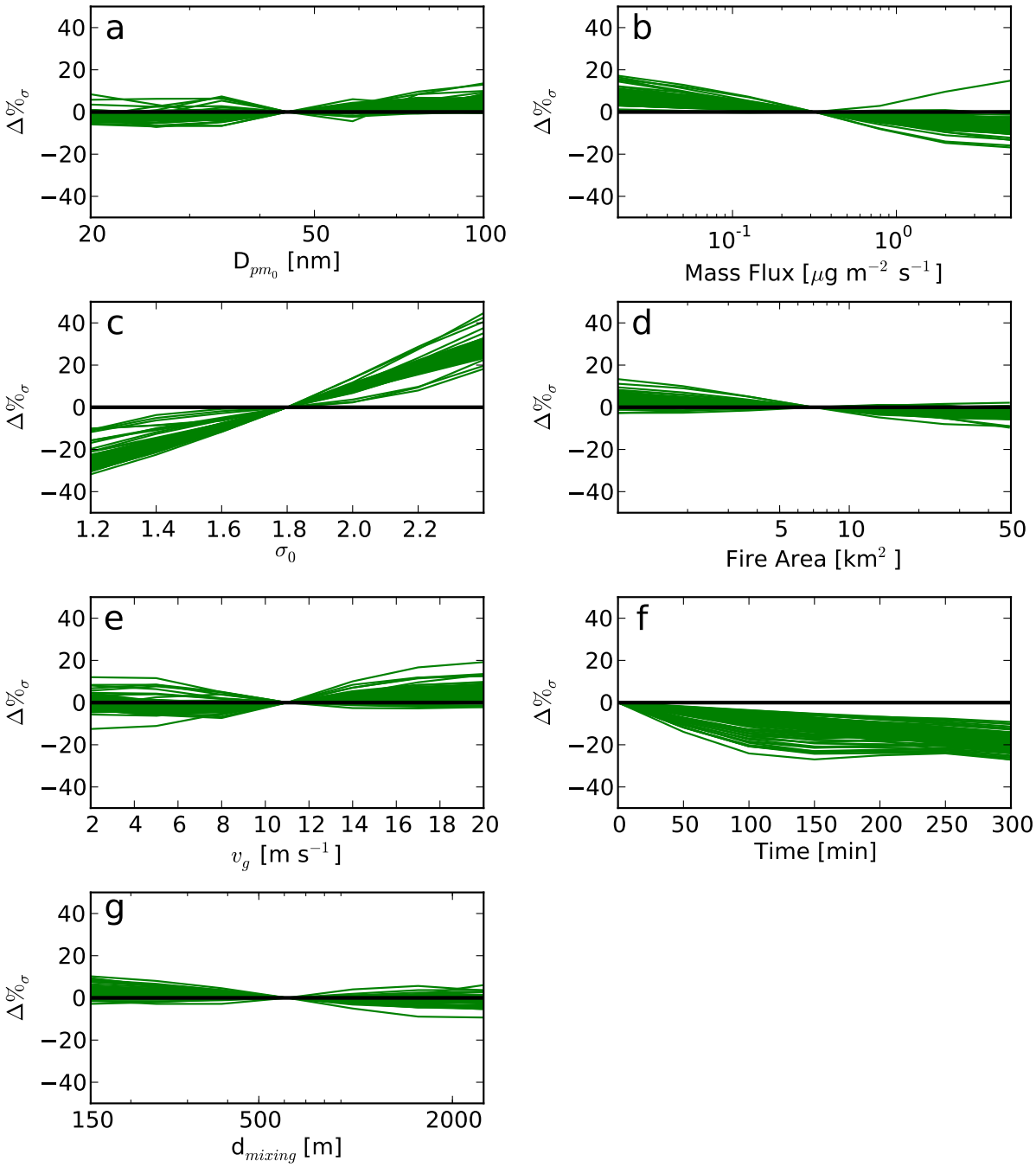

FIGURE 3.8. Sensitivity plots for the 7 input parameters to the GEM-SA σ emulator parameterization. One hundred random input sets (non-training data) were used. The sensitivities are shown as percent change in final σ, individually normalized to the center value of the x-axis (to zero in Time).

The emulator-derived σ sensitivities are shown in Figure 3.8. Since we expect σ to converge towards an asymptotic limit with coagulational processing (Figure 3.4b-d), we see with those input parameters associated with higher total emissions (Mass flux, Fire area, v_g^{-1}, mixing depth^{-1}), which gave monotonic increases/decreases for D_{pm}, show mixed results for σ due to variability in the initial σ_0. The time sensitivity plot (Figure 3.8f) shows decreasing σ with time similar to Figure 3.4b,d.

Emission σ_0 shows the most pronounced and largest magnitude effect on output σ ($\sim$100%). Thus, the timescales for σ evolving towards 1.2 is longer than the timescales tested here for even the densest plumes. These sensitivity plots show there is much less variability in σ ($\pm$ 50%) than in D_{pm} over the tested input space. Overall, the GEM-SA estimates that 81% of D_{pm} variability and 87% of σ variability are captured by these seven inputs.

3.3.4 Simplified fits to the aged size-distributions

In addition to the GEM-SA emulator fits, we present simplified fits for both D_{pm} and σ based on the behaviour in Figures 3.4-3.5 (see Section 3.3.1). These fits are easier to implement in regional and global aerosol models. These equations are meant to produce approximate estimates of D_{pm} and σ throughout plume size-distribution aging. The equations require three input parameters: the initial value of the size-parameter of interest (D_{pm_0} or σ_0), a value proportional to the plume aerosol loading (dM/dxdz: Mass flux $\times$ Fire area / v_g / mixing depth or dM/dx: Mass flux $\times$ Fire area / v_g), and distance from the source fire (distance). The functional forms fitted for D_{pm} and σ are found below.

(3.1a) $$D_{pm} = D_{pm_0} + A\left(\frac{dM}{dx}\right)^b (distance)^c$$

(3.1b) $$D_{pm} = D_{pm_0} + A\left(\frac{dM}{dxdz}\right)^b (distance)^c$$

(3.2a) $$\sigma = \sigma_0 + A\left(\frac{dM}{dx}\right)^b (distance)^c (1.2 - \sigma_0)$$

(3.2b) $$\sigma = \sigma_0 + A\left(\frac{dM}{dxdz}\right)^b (distance)^c (1.2 - \sigma_0)$$

TABLE 3.3. Simplified D_{pm} and σ SAM-TOMAS fit parameters

Fit	*Ref.*	*Parameter*		
		A	*b*	*c*
D_{pm}(dM/dx)	3.1a	11.33	0.4389	0.3477
D_{pm}(dM/dxdz)	3.1b	289.8	0.4514	0.3563
σ(dM/dx)	3.2a	0.09519	0.2579	0.3127
σ(dM/dxdz)	3.2b	0.5140	0.2411	0.3396

where A, b and c are determined by fitting each equation to the SAM-TOMAS data. For these empirical equations, the units of dM/dx are kg m^{-1}, dM/dxdz are kg m^{-2}, D_{pm} is nm and distance is km. It should be noted that the equations for D_{pm} and σ are designed to be independent of each other (i.e. D_{pm} is not dependent on σ_0), which differs from the GEM-SA emulator (see Section 3.4.3). The aerosol loading parameter dM/dx was chosen based on the stratification seen in Figures 3.4c and 3.5. dM/dxdz (Mass flux × Fire area/(v_g d_{mixing})) was tested as well, as it incorporates the variance associated with mixing depth into the fit. Because we expect mixing depth of the plume to be one of the more uncertain parameters in an atmospheric model, and the D_{pm} and σ sensitivities to d_{mixing} tend to be low in comparison to the other factors tested in the GEM-SA emulator (see Section 3.4.3), the fit to dM/dx rather than dM/dxdz may be advantageous. The σ fits introduce a fourth factor, (1.2-σ_0), which represents the difference between the SAM-TOMAS coagulational limit (Figure 3.4b and d) and the initial modal width.

The scalar A, b and c variables were fit to the ensemble SAM-TOMAS data via an objective function. Their values are summarized in Table 3.3. The fits were tested against independent data in Figures 3.9 (D_{pm}) and 3.10 (σ). The simplified D_{pm} parameterizations, as expected, are not as good a fit of the SAM-TOMAS data as the GEM-SA emulator (dm/dx: slope = 0.75, R^2 = 0.6, MNB= 0.01, dM/dxdz: slope = 0.93, R^2 = 0.71, MNB= 0.04), with the fit incorporating dM/dxdz performing better than that with dM/dx. The simple σ fit also did not perform as well as the GEM-SA emulator (dm/dx: slope = 0.64, R^2 = 0.73, MNB= 0.01, dM/dxdz: slope = 0.64, R^2 = 0.74, MNB= 0.005). Thus, dM/dxdz fits do yield better results than dM/dx (in particular for D_{pm}); however, a user may choose to use the dM/dx fit if the mixing depth is unknown.

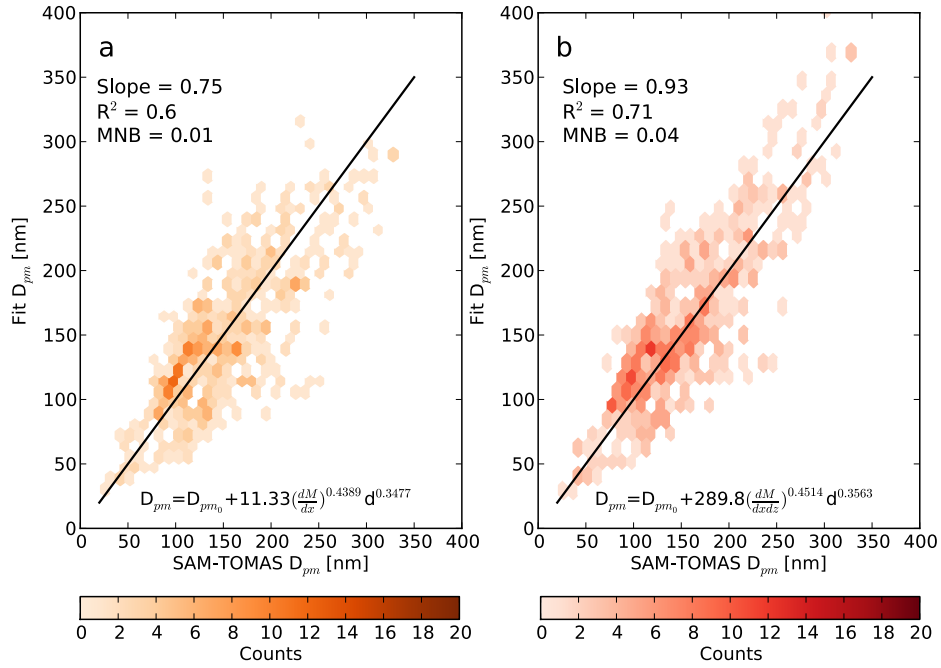

FIGURE 3.9. One-to-one plot showing SAM-TOMAS vs the simplified D_{pm} fit for a) dM/dx, and b) dM/dxdz. The black line is the one-to-one line. N = 624pts.

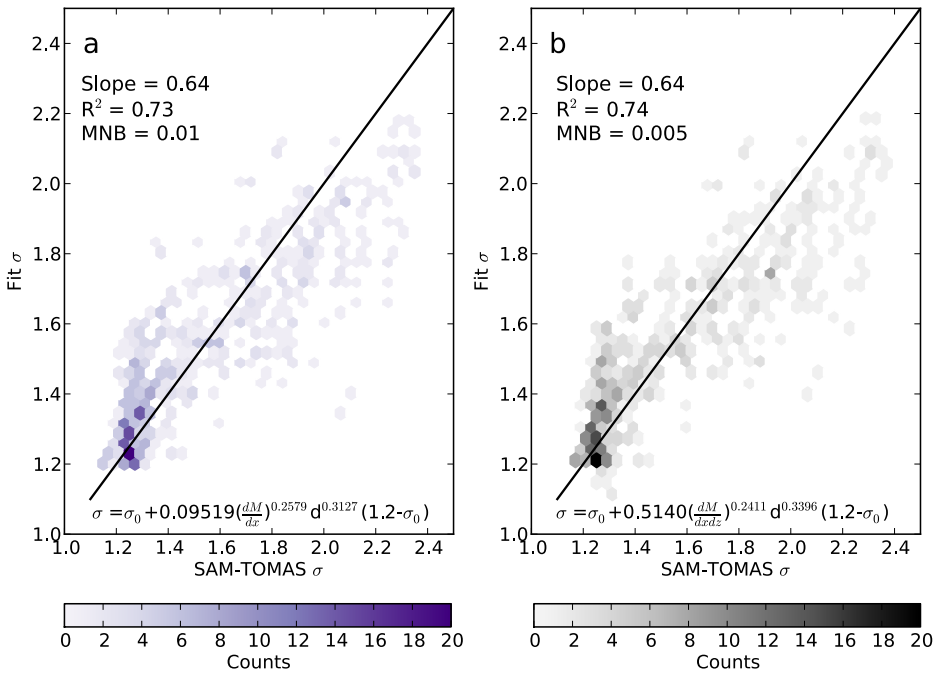

FIGURE 3.10. One-to-one plot showing SAM-TOMAS vs the simplified σ fit for a) dM/dx, and b) dM/dxdz. The black line is the one-to-one line. N = 624pts.

3.3.5 Accounting for OA production/losses

One of the limitations of a coagulation-only parameterization is that it does not include the effects of potential condensation/evaporation of organic aerosol on the aged biomass-burning size distribution. Both condensational growth and evaporative loss of organic aerosol through organic compounds has been observed previously in chamber studies due to OA production or evaporation from dilution (Hennigan et al., 2011; Grieshop et al., 2009). The amount of net OA production/loss within BB plumes is variable, with numerous field studies observing SOA production (Cubison et al., 2011; Hecobian et al., 2011), while others document little or no net SOA production (Capes et al., 2008; Sakamoto et al., 2014). With this range in net OA production/loss, it is difficult to constrain the plume size-distribution's capacity for condensational growth or evaporative shrinking as it ages.

Here we present how we expect the parameterization to change based on in-plume OA production/loss. If a parameterization user expects OA production or loss in a plume, they may use the simple corrections of our parameters below. We assume that the OA production or loss does not affect the coagulation rates or σ, but just acts to increase the final D_{pm}. For large changes in OA mass (more than a factor of 2) due to production/loss, our simple correction will have uncertainties due to these assumptions. Our correction to the final D_{pm} has the following form:

$$D_{pm_{\text{w/ OAprod/loss}}} = D_{pm_{\text{w/o OAprod/loss}}} \times \left(\frac{OAMass_{\text{w/ OAprod/loss}} + BCMass}{OAMass_{\text{w/o OA prod/loss}} + BCMass} \right)^{\frac{1}{3}} \tag{3.3}$$

where $D_{pm_{\text{w/o OAprod/loss}}}$ is the final D_{pm} from the coagulation-only GEM-SA emulator parameterization, the BB aerosol OA mass (with and without additional production or loss) is in kg and the BC mass is in kg. Thus, for a doubling of OA due to SOA production (one of the larger enhancements found in Hennigan et al., 2011), particles that contain negligible BC will grow in diameter by 26% above the coagulation-only predictions. If the particles contained

50% BC, then the diameter growth would only be 14%. It should be noted that the D_{pm} growth attributed to OA condensation is not accompanied by an increase in particle number (additional OA mass is distributed among existing particles). Whereas a similar increase in D_{pm} growth by coagulation only would have an accompanying decrease in particle number.

While these changes are expected to be on the large end for growth by SOA production, they are significantly smaller than the ~200% range D_{pm} changes over the range of initial fire conditions due to coagulation alone shown earlier (Figures 3.7-3.8). For instance, variations in windspeed and fire area alone can independently cause shifts in D_{pm} of 100% due to changes in coagulation rates. This indicates that although SOA condensational growth is certainly important from a compositional and total-mass standpoint, it is not among the most dominant factors driving the aged D_{pm} size-distribution compared to those fire-condition parameters controlling coagulational growth.

3.4 Conclusions

3.4.1 Summary

We used the SAM-TOMAS large-eddy model and an emulation technique to explore the evolution of biomass-burning aerosol size distributions and build a coagulation-only D_{pm} and σ parameterization of this evolution. We have also provided a simple correction to the parameterization for cases with net OA production or loss. We used the SAM-TOMAS model to simulate plume dispersion and aerosol coagulation. The SAM-TOMAS results show that the aged D_{pm} can be largely described by dM/dx (Mass flux × Fire area/v_g, or the mass of particles in a slice of air normal to the mean wind) and the distance from the source. These results also show that the aged σ moves from σ_0 towards a value of 1.2 at a rate that depends on dM/dx.

The GEM-SA program was used to derive a seven-input D_{pm} and σ parameterization based on the SAM-TOMAS results. The parameterization requires seven input parameters: emission D_{pm_0}, emission σ_0, mass flux, boundary layer windspeed (v_g), fire area, plume mixing depth, and time. The predicted D_{pm} and σ, which have captured the sub-grid coaguational

growth, can then be used as effective unimodal BB size-distribution parameters in regional and global aerosol models.

The D_{pm} parameterization showed the strongest sensitivities to those input parameters associated with the extent of aerosol loading within the plume (mass flux, fire area, v_g). Across the mass flux, fire area, and v_g ranges tested here, final D_{pm} varied by between 120–200%. This is consistent with dM/dx (a measure of aerosol loading) stratification with D_{pm} growth seen in Figure 3.4c. These sensitivities were larger than those associated with mixing depth (∼40%) or the initial size-distribution parameters (D_{pm_0} max. 100% , σ_0 max. 50%). The σ parameterization shows a uniform decrease with time and strong sensitivities to emission σ_0 (∼250%) . The 100% variance in σ as a result of σ_0 can be attributed to the inertia in σ evolution those simulations with large modal widths and relatively small mass loading will not converge quickly to the coagulational limit (1.2).

The parameterization performs relatively well against the SAM-TOMAS model with good correlation, slope and a low mean normalized biases for D_{pm} (R^2= 0.83, slope= 0.92, MNB= -0.06) and σ (R^2= 0.93, slope= 0.91, MNB= 0.01). The σ parameterization seems unable to capture the coagulational limit of 1.2 seen in the SAM-TOMAS results. This 1.2 limit differs from the 1.32 σ limit proposed by Lee (1983) likely due to the bin-spacing in SAM-TOMAS being coarser than lognormal modes with these small modal widths.

This parameterization is based on coagulation-only SAM-TOMAS simulations and assumes no in-plume condensation of SOA. The correction for OA production/loss discussed in Section 3.3.4 indicates that significant production of SOA within the plume (∼100% OA mass enhancement) would cause a relatively small shift in the size-distribution D_{pm} (14-26% increase) compared to other factors (e.g. fire conditions). The simplified correction assumes no change in σ with condensational growth. Further testing should be done with explicit OA production and loss to better quantify the effects of condensation of the size-distribution evolution.

The lack of water uptake in this version of the parameterization means it is unable to simulate any cloud-processing that may occur in-plume. Our analysis does not include any

cloud processing of the plume particles, i.e. the production of aqueous SOA within activated plume particles is not accounted for in our simple OA mass correction. The production of SOA within droplets could result in additional SOA mass being only added to the larger, activated particles during activation/evaporation cycling. This extra SOA mass would favor increases in the diameters of the larger particles of the size-distribution only, which would create a bimodal size distribution and increase the overall coagulational rates in the plume (more, larger particles coagulate more rapidly with the small-diameter particles).

The next steps for this work are (1) testing the parameterizations developed in this work against real world observations of size distribution aging, and (2) incorporating the parameterizations into regional and global aerosol models for further evaluation against regional/global measurements. Testing the parameterizations against measurements from field campaigns where both fresh and aged sampled aerosol size distributions were measured (ideally with multiple transects and precise transport times) will provide the ideal test cases.

4. Conclusions and Recommendations

4.1 Conclusions

In this project, we investigated biomass-burning aerosol size distributions from an observational and theoretical modelling standpoint. In chapter 2, aged biomass-burning plume samples from BORTAS-B were analysed to characterize the aged aerosol size-distribution associated with the boreal wildfires. We also made a secondary analysis of the BORTAS-B data using a box-model to simulate the evolution of the aged size distributions and estimate the associated fresh-plume size-distributions. In chapter 3, we perform a theoretical investigation of the factors contributing to aging of biomass-burning size distributions. This included building parameterizations suitable for insertion in larger-gridbox atmospheric models. Both the observational and modelling sections of this study were designed to better the understanding of how aerosol size-distributions from biomass-burning evolve in the atmosphere.

Chapter 2 of this study focused on the analysis of aircraft-sampled aged biomass-burning plumes during BORTAS-B (see Palmer et al. (2013); Parrington et al. (2013); Taylor et al. (2014) for more). Two research flights sampled highly concentrated BB plumes (∼400–11200 km downwind) from source fires in Northwestern Ontario. The identification of the plumes was determined by implementing threshold concentrations across four biomass-burning tracers sampling simultaneously: carbon monoxide ($[CO]_{thresh}$=150 ppbv), acetonitrile ($[CH_3CN]_{thresh}$=200 pptv), organic aerosol ($[OA]_{thresh}$=20 μgm^{-3}), and black carbon ($[BC]_{thresh}$= 50 m^{-3}). These thresholds are 1.5 the background concentrations in each case. The plumes were highly concentrated and there was very good correlation between all four tracers during both flights.

The organic enhancement ratios ($\Delta OA/\Delta CO$) were calculated for different transects (sections of in-plume sampling) for flight b622. The enhancement ratios showed a pronounced altitude dependence, with samples taken at altitudes >4.6 km having much less ΔOA than expected for these plumes. We filtered these points for the remainder of our analysis, citing Franklin et al. 2014 that attributed the low OA in the high plume to rainout along the

transport route. The enhancement ratios for those samples below 4.6 km were consistent for each transect (0.05–0.18 μg m^{-3}ppbv^{-1}) with high correlation coefficients (8 of 9 had R^2>0.5). They did not show any significant trend above the noise with distance from the source fires, which would have indicated either OA production or loss within the plume. We conclude therefore, that no significant net OA production/loss occurred across the distances observed (however, production/loss may have occurred earlier in the plume).

The BB plume size-distributions were measured by SMPS and showed little variation across the flights, or with altitude. The composite BB size-distribution had a single accumulation mode with fitted lognormal parameters: D_{pm}= 230 nm and σ= 1.5, which is comparable to other measurement of aged smoke found in the literature (Kondo et al., 2011; Capes et al., 2008; Janhäll et al., 2010). The BB size-distribution also had higher concentrations of small diameter particles (20–90 nm), which was unexpected. A coagulation calculation showed the coagulational lifetime of these particles is quite short (∼8 hours), and we would have expected removal by the accumulation mode particles to lead to low concentrations at these smaller diameters than what was measured by the SMPS. The cause of this elevated 'tail' in the characteristic plume size-distribution is unexplained.

We modelled the past-evolution of the aged characteristic size-distribution with a Lagrangian box-model. The model output was then compared to the composite BORTAS-B size-distribution to determine the optimal fresh-plume size-distribution associated with the aged aerosol observed by the SMPS. The box-model simulates coagulation and dilution (by e-folding volume exchange) only. Condensation was omitted since no SOA production was detected in the analysed plume. The dilution rate of the plume was unknown, so a variety of dilution coefficients were tested (τ_{dil} =24, 36, 48 hrs). The model had a runtime of 48 hrs based on the maximum physical transport age of the plume.

Coagulational growth within the concentrated plume caused rapid modelled growth of the size-distribution particles within the first 10 hrs of aging (80% of total D_{pm}). This rapid rate is due to the coagulation rate dependence on N^2. The associated optimal fresh plume size-distribution parameters were highly dependent on τ_{dil} with parameters ranging

from D_{pm}=67–97 nm and σ=2.4-1.7 (for τ_{dil} ranging from 24–48 hrs). The shorter τ_{dil} rates ($\sim$20–36 hrs) have modelled fresh-plume size-distributions very similar to those observed in field studies of fresh BB aerosol (Janhäll et al., 2010) and indicate that even such a simple coagulation-only box model can capture the general evolution behavior of BB plumes.

In Chapter 3, a separate theoretical study of size-distribution evolution involved investigating the factors contributing to the variance in BB size-distribution aging. We built and tested a coagulation-only parameterization of single-mode aged BB size-distributions (characterized by D_{pm} and σ). The parameterization accepts 7 inputs related to: the initial fresh BB size distribution (D_{pm_0}, σ_0), the fire conditions (mass flux, fire area), local meteorology (windspeed (v_g), aerosol mixing depth (d_{mixing})), and time.

SAM-TOMAS, a large-eddy model with online aerosol microphysics, was used as the base model since it has a resultion capable of resolving the plume dispersion of larger fires(500 m $\times$ 500 m $\times$ 40 m) and is capable of explicitly tracking and processing plume size-distributions across 15 bins (range: 3 nm - 10 μm). Coagulation was the only microprocess considered (no condensation, water uptake/ aqueous processing or nucleation) since it was found to be the dominant process in the BORTAS-B plume study (Chapter 2) and the attributable variance in D_{pm} and σ was expected to be larger than that from condensation. We explore the potential effects of OA production/loss later in the chapter. The modelled BB particles were a uniform density and non-hygroscopic for simplicity.

We found that the SAM-TOMAS model output showed trends in D_{pm} and σ in each simulation. D_{pm} grew as time increased, with dD_{pm}/dt dependent on dM/dx (mass flux $\times$ fire area/v_g). This suggests that those plumes with higher aerosol loading will both reach higher final D_{pm} and will do so at a faster dD_{pm}/dt rate. Modal width (σ) approached, but generally did not reach, a coagulational limit of $\sim$1.2 with time. We provided simplified fits based on this output for D_{pm} and σ. To improve on these simplified fits, we used a gaussian emulator (generated by GEM-SA software) as a statistical estimator for the SAM-TOMAS model and to build the final parameterizations of D_{pm} and σ.

With the GEM-SA-derived emulator, the high correlations and low bias errors suggest that the seven parameters chosen were adequate for capturing the majority of the variance in D_{pm} and σ for this experimental set-up. We used sensitivity plots to understand the contributions of each of the input parameters to the output (D_{pm} or σ) variance. We found that parameters associated with higher aerosol loading show strong monotonic trends in both + D_{pm} and - σ. Across realistic input ranges we found sensitivities in D_{pm} of up to 200% (mass flux) and in σ of up to 140 % (σ_0). We suggest therefore, that fire conditions (mass flux, fire area) as well as wind speed and σ_0 are the dominant factors in determining coagulational evolution.

The emulator parameterization is limited in assuming no in-plume chemistry. We expect OA production/loss within the plume to contribute to the condensational growth/shrinking of the size distribution, and we provide a simple correction of OA production/loss to our parameterizations. However, our simplified correction shows that significant SOA mass production/loss (of $\sim\Delta$100% OA mass production) would only change D_{pm} by a factor of $\sim\pm$ 14-26%. This is much smaller than the D_{pm} variance in the coagulation-only scenario attributed to fire condition factors such as mass flux ($\sim$200%). This parameterization is additionally limited by ideal conditions, with no wet/dry deposition of aerosol particles, diameter growth via water uptake or aqeous SOA formation.

4.2 Recommendations

Though the GEM–SA parameterizations of D_{pm} and σ performed quite well against the SAM-TOMAS model, an independent, complete dataset of observed BB size distributions would be ideal for testing against the predicted parameterizations. The observed dataset would require fitted D_{pm} and σ measurements at numerous times for the same BB plume of known source fire conditions (fuel type, fire area, etc.). This would enable a real-world comparison between the parameterizations and observed data.

Further SAM-TOMAS testing with OA condensation/evaporation and estimates of how aqueous SOA could potentially affect the size-distribution would also be useful. This would

involve constraining the amount and timing condensable material within the plume. Modelling the effects of aqueous SOA would require allowing water uptake and activation of the particles, and inserting an aqueous SOA production yield as a function atmospheric conditions. Evaluating how these schemes affect the parameterizations (relative to the coagulation-only scheme) would help quantify relative dominance of microphysical processes on aerosol size evolution.

We recommend for future investigations that the D_{pm} and σ parameterizations in chapter 3 are embedded in a global aerosol model to assess the changes in the aerosol size distribution as well as climate forcings. GEOS-CHEM is a large-grid global chemical transport model that handles aerosol size through TOMAS microphysics, making it an ideal aerosol model to test the parameterizations. The study would take advantage of current global BB inventories (e.g. GFED3, FINN; which include mass flux and fire area estimates) to evaluate the regional and global changes in CCN concentrations and aerosol climate forcings with the parameterized aged-plume size distributions (from D_{pm} and σ) versus the current, globally uniform biomass-burning emissions size distributions.

References

Adams, P. J. and Seinfeld, J. H. (2002). Predicting global aerosol size distributions in general circulation models. *Journal of Geophysical Research-Atmospheres*, 107(D19):4310–4370.

Alonso-Blanco, E. (2014). Impact of Biomass Burning on Aerosol Size Distribution, Aerosol Optical Properties and Associated Radiative Forcing. *Aerosol and Air Quality Research*, 006:708–724.

Andreae, M. O., Artaxo, P., Fischer, H., Freitas, S. R., Grégoire, J.-M., Hansel, a., Hoor, P., Kormann, R., Krejci, R., Lange, L., Lelieveld, J., Lindinger, W., Longo, K., Peters, W., de Reus, M., Scheeren, B., Silva Dias, M. a. F., Ström, J., van Velthoven, P. F. J., and Williams, J. (2001). Transport of biomass burning smoke to the upper troposphere by deep convection in the equatorial region. *Geophysical Research Letters*, 28(6):951–954.

Andreae, M. O. and Merlet, P. (2001). Emission of trace gases and aerosols from biomass burning. *Global Biogeochemical Cycles*, 15(4):955–966.

Bauer, S. E., Menon, S., Koch, D., Bond, T. C., and Tsigaridis, K. (2010). A global modeling study on carbonaceous aerosol microphysical characteristics and radiative effects. *Atmospheric Chemistry and Physics*, 10(15):7439–7456.

Boucher, O. (2000). Estimates of the direct and indirect radiative forcing due to tropospheric aerosols: A review. (1999):513–543.

Capes, G., Johnson, B., McFiggans, G., Williams, P. I., Haywood, J., and Coe, H. (2008). Aging of biomass burning aerosols over West Africa: Aircraft measurements of chemical composition, microphysical properties, and emission ratios. *Journal of Geophysical Research*, 113:D00C15.

Carrico, C. M., Petters, M. D., Kreidenweis, S. M., Sullivan, A. P., McMeeking, G. R., Levin, E. J. T., Engling, G., Malm, W. C., and Collett, J. L. (2010). Water uptake and chemical composition of fresh aerosols generated in open burning of biomass. *Atmospheric Chemistry and Physics*, 10(11):5165–5178.

Chen, W.-T., Lee, Y. H., Adams, P. J., Nenes, a., and Seinfeld, J. H. (2010). Will black carbon mitigation dampen aerosol indirect forcing? *Geophysical Research Letters*, 37(9):L09801.

Cubison, M. J., Ortega, a. M., Hayes, P. L., Farmer, D. K., Day, D., Lechner, M. J., Brune, W. H., Apel, E., Diskin, G. S., Fisher, J. a., Fuelberg, H. E., Hecobian, a., Knapp, D. J., Mikoviny, T., Riemer, D., Sachse, G. W., Sessions, W., Weber, R. J., Weinheimer, a. J., Wisthaler, a., and Jimenez, J. L. (2011). Effects of aging on organic aerosol from open biomass burning smoke in aircraft and laboratory studies. *Atmospheric Chemistry and Physics*, 11(23):12049–12064.

DeCarlo, P. F., Ulbrich, I. M., Crounse, J., de Foy, B., Dunlea, E. J., Aiken, a. C., Knapp, D., Weinheimer, a. J., Campos, T., Wennberg, P. O., and Jimenez, J. L. (2010).

Investigation of the sources and processing of organic aerosol over the Central Mexican Plateau from aircraft measurements during MILAGRO. *Atmospheric Chemistry and Physics*, 10(12):5257–5280.

Engelhart, G. J., Hennigan, C. J., Miracolo, M. a., Robinson, a. L., and Pandis, S. N. (2012). Cloud condensation nuclei activity of fresh primary and aged biomass burning aerosol. *Atmospheric Chemistry and Physics*, 12(15):7285–7293.

Franklin, J. E., Drummond, J. R., Griffin, D., Pierce, J. R., Waugh, D. L., Palmer, P. I., Parrington, M., Lee, J. D., Lewis, a. C., Rickard, a. R., Taylor, J. W., Allan, J. D., Coe, H., Walker, K. a., Chisholm, L., Duck, T. J., Hopper, J. T., Blanchard, Y., Gibson, M. D., Curry, K. R., Sakamoto, K. M., Lesins, G., Dan, L., Kliever, J., and Saha, a. (2014). A case study of aerosol scavenging in a biomass burning plume over eastern Canada during the 2011 BORTAS field experiment. *Atmospheric Chemistry and Physics*, 14(16):8449–8460.

Freitas, S. R., Longo, K. M., Chatfield, R., Latham, D., Dias, M. A. F. S., Andreae, M. O., Prins, E., and Unesp, F. E. G. (2007). Including the sub-grid scale plume rise of vegetation fires in low resolution atmospheric transport models. *Atmospheric Chemistry and Physics*, pages 3385–3398.

Fuchs, N. A. (1964). *The Mechanics of Aerosols*. Oxford: Pergamon Press.

Grieshop, A. P., Logue, J. M., Donahue, N. M., and Robinson, A. L. (2009). Laboratory investigation of photochemical oxidation of organic aerosol from wood fires 1: measurement and simulation of organic aerosol evolution. *Atmospheric Chemistry and Physics*, 9(4):1263–1277.

Hecobian, A., Liu, Z., Hennigan, C. J., Huey, L. G., Jimenez, J. L., Cubison, M. J., Vay, S., Diskin, G. S., Sachse, G. W., Wisthaler, A., Mikoviny, T., Weinheimer, A. J., Liao, J., Knapp, D. J., Wennberg, P. O., Kürten, A., Crounse, J. D., Clair, J. S., Wang, Y., and Weber, R. J. (2011). Comparison of chemical characteristics of 495 biomass burning plumes intercepted by the NASA DC-8 aircraft during the ARCTAS/CARB-2008 field campaign. *Atmospheric Chemistry and Physics*, 11(24):13325–13337.

Hennigan, C. J., Miracolo, M. a., Engelhart, G. J., May, a. a., Presto, a. a., Lee, T., Sullivan, a. P., McMeeking, G. R., Coe, H., Wold, C. E., Hao, W.-M., Gilman, J. B., Kuster, W. C., de Gouw, J., Schichtel, B. a., Kreidenweis, S. M., and Robinson, a. L. (2011). Chemical and physical transformations of organic aerosol from the photo-oxidation of open biomass burning emissions in an environmental chamber. *Atmospheric Chemistry and Physics*, 11(15):7669–7686.

Hennigan, C. J., Westervelt, D. M., Riipinen, I., Engelhart, G. J., Lee, T., Collett, J. L., Pandis, S. N., Adams, P. J., and Robinson, A. L. (2012). New particle formation and growth in biomass burning plumes: An important source of cloud condensation nuclei. *Geophysical Research Letters*, 39(9):n/a–n/a.

Heringa, M. F., DeCarlo, P. F., Chirico, R., Tritscher, T., Dommen, J., Weingartner, E., Richter, R., Wehrle, G., Prévôt, a. S. H., and Baltensperger, U. (2011). Investigations of

primary and secondary particulate matter of different wood combustion appliances with a high-resolution time-of-flight aerosol mass spectrometer. *Atmospheric Chemistry and Physics*, 11(12):5945–5957.

Hobbs, P. V., Sinha, P., Yokelson, R. J., Christian, T. J., Blake, D. R., Gao, S., Kirchstetter, T. W., Novakov, T., and Pilewskie, P. (2003). Evolution of gases and particles from a savanna fire in South Africa. *Journal of Geophysical Research*, 108(D13).

Holzinger, R., Williams, J., Salisbury, G., Klüpfel, T., de Reus, M., Traub, M., Crutzen, P. J., and Lelieveld, J. (2005). Oxygenated compounds in aged biomass burning plumes over the Eastern Mediterranean: evidence for strong secondary production of methanol and acetone. *Atmospheric Chemistry and Physics*, 5(1):39–46.

Hosseini, S., Li, Q., Cocker, D., Weise, D., Miller, a., Shrivastava, M., Miller, J. W., Mahalingam, S., Princevac, M., and Jung, H. (2010). Particle size distributions from laboratory-scale biomass fires using fast response instruments. *Atmospheric Chemistry and Physics*, 10(16):8065–8076.

Hudson, P. K., Murphy, D. M., Cziczo, D. J., Thomson, D. S., de Gouw, J. A., Warneke, C., Holloway, J., Jost, H.-J., and Hübler, G. (2004). Biomass-burning particle measurements: Characteristic composition and chemical processing. *Journal of Geophysical Research*, 109(D23):D23S27.

Jacobson, M. Z. (2001). Strong radiative heating due to the mixing state of black carbon in atmospheric aerosols. *Nature*, 409(6821):695–697.

Janhäll, S., Andreae, M. O., and Pöschl, U. (2010). Biomass burning aerosol emissions from vegetation fires : particle number and mass emission factors and size distributions. *Atmos. Chem. Phys*, pages 1427–1439.

Kennedy, M., Anderson, C., O'Hagan, A., Lomas, M., Woodward, I., Gosling, J. P., and Heinemeyer, A. (2008). Quantifying uncertainty in the biospheric carbon flux for england and wales. *Journal of the Royal Statistical Society: Series A (Statistics in Society)*, 171(1):109–135.

Kennedy, M. and O'Hagan, A. (2001). Bayesian calibration of computer models. *J. R. Stat. Soc. Ser. B Stat. Methodol.*, 63(3):425–464.

Khairoutdinov, M. F. and Randall, D. A. (2003). Cloud resolving modeling of the ARM summer 1997 IOP: Model formulation, results, uncertainties, and sensitivities. *Journal of the Atmospheric Sciences*, 60(4):607–625.

Klug, W. (1969). A method for determining diffusion conditions from synoptic observations. *Staub-Reinhalt. Luft*, 29:14–20.

Kondo, Y., Matsui, H., Moteki, N., Sahu, L., Takegawa, N., Kajino, M., Zhao, Y., Cubison, M. J., Jimenez, J. L., Vay, S., Diskin, G. S., Anderson, B., Wisthaler, a., Mikoviny, T., Fuelberg, H. E., Blake, D. R., Huey, G., Weinheimer, a. J., Knapp, D. J., and Brune, W. H. (2011). Emissions of black carbon, organic, and inorganic aerosols from biomass

burning in North America and Asia in 2008. *Journal of Geophysical Research*, 116(D8):D08204.

Lee, K. (1983). Change of particle size distribution during brownian coagulation. *Journal of Colloid and Interface Science*, 92(2):315 – 325.

Lee, L. a., Carslaw, K. S., Pringle, K. J., and Mann, G. W. (2012). Mapping the uncertainty in global CCN using emulation. *Atmospheric Chemistry and Physics*, 12(20):9739–9751.

Lee, L. a., Carslaw, K. S., Pringle, K. J., Mann, G. W., and Spracklen, D. V. (2011). Emulation of a complex global aerosol model to quantify sensitivity to uncertain parameters. *Atmospheric Chemistry and Physics*, 11(23):12253–12273.

Lee, L. A., Pringle, K. J., Reddington, C. L., Mann, G. W., Stier, P., Spracklen, D. V., Pierce, J. R., and Carslaw, K. S. (2013). The magnitude and causes of uncertainty in global model simulations of cloud condensation nuclei. *Atmospheric Chemistry and Physics*, 13(17):8879–8914.

Lee, S., Kim, H. K., Yan, B., Cobb, C. E., Hennigan, C., Nichols, S., Chamber, M., Edgerton, E. S., Jansen, J. J., Hu, Y., Zheng, M., Weber, R. J., and Russell, A. G. (2008). Diagnosis of aged prescribed burning plumes impacting an urban area. *Environmental science & technology*, 42(5):1438–44.

Leppä, J., Mui, W., Grantz, A. M., and Flagan, R. C. (2014). Importance of charger ion properties in size distribution measurements. International Aerosol Conference.

Levin, E. J. T., McMeeking, G. R., Carrico, C. M., Mack, L. E., Kreidenweis, S. M., Wold, C. E., Moosmüller, H., Arnott, W. P., Hao, W. M., Collett, J. L., and Malm, W. C. (2010). Biomass burning smoke aerosol properties measured during Fire Laboratory at Missoula Experiments (FLAME). *Journal of Geophysical Research*, 115(D18):D18210.

Lonsdale, C. R., Stevens, R. G., Brock, C. a., Makar, P. a., Knipping, E. M., and Pierce, J. R. (2012). The effect of coal-fired power-plant SO¡sub¿2¡/sub¿ and NO¡sub¿x¡/sub¿ control technologies on aerosol nucleation in the source plumes. *Atmospheric Chemistry and Physics*, 12(23):11519–11531.

López-Yglesias, X. and Flagan, R. C. (2013). Ionaerosol flux coefficients and the steady-state charge distribution of aerosols in a bipolar ion environment. *Aerosol Sci. Tech.*, 47(30):688–704.

McMeeking, G. R., Kreidenweis, S. M., Baker, S., Carrico, C. M., Chow, J. C., Collett, J. L., Hao, W. M., Holden, A. S., Kirchstetter, T. W., Malm, W. C., Moosmüller, H., Sullivan, A. P., and Wold, C. E. (2009). Emissions of trace gases and aerosols during the open combustion of biomass in the laboratory. *Journal of Geophysical Research*, 114(D19):D19210.

Myhre, G., Shindell, D., Bron, F.-M., Collins, W., Fuglestvedt, J., Huang, J., Koch, D., Lamarque, J.-F., Lee, D., Mendoza, B., Nakajima, T., Robock, A., Stephens, G.,

Takemura, T., and Zhang, H. (2013). *Climate Change 2013: The Physical Science Basis*, chapter Anthropogenic and Natural Radiative Forcing: Contribution of Working Group I to the Fifth Assessment Report of the Intergovernmental Panel on Climate Change. Cambridge University Press.

Okoshi, R., Rasheed, A., Chen Reddy, G., McCrowey, C. J., and Curtis, D. B. (2014). Size and mass distributions of ground-level sub-micrometer biomass burning aerosol from small wildfires. *Atmospheric Environment*, 89:392–402.

Ontario Ministry of Natural Resources and Forestry (2012). 2011 Forest Fire Summary. Available at https://www.ontario.ca/law-and-safety/forest-fires.

Ortega, a. M., Day, D. a., Cubison, M. J., Brune, W. H., Bon, D., de Gouw, J. a., and Jimenez, J. L. (2013). Secondary organic aerosol formation and primary organic aerosol oxidation from biomass-burning smoke in a flow reactor during FLAME-3. *Atmospheric Chemistry and Physics*, 13(22):11551–11571.

Palmer, P. I., Parrington, M., Lee, J. D., Lewis, A. C., Rickard, A. R., Bernath, P. F., Duck, T. J., Waugh, D. L., Tarasick, D. W., Andrews, S., Aruffo, E., Bailey, L. J., Barrett, E., Bauguitte, S. J.-B., Curry, K. R., Di Carlo, P., Chisholm, L., Dan, L., Forster, G., Franklin, J. E., Gibson, M. D., Griffin, D., Helmig, D., Hopkins, J. R., Hopper, J. T., Jenkin, M. E., Kindred, D., Kliever, J., Le Breton, M., Matthiesen, S., Maurice, M., Moller, S., Moore, D. P., Oram, D. E., O'Shea, S. J., Owen, R. C., Pagniello, C. M. L. S., Pawson, S., Percival, C. J., Pierce, J. R., Punjabi, S., Purvis, R. M., Remedios, J. J., Rotermund, K. M., Sakamoto, K. M., da Silva, A. M., Strawbridge, K. B., Strong, K., Taylor, J., Trigwell, R., Tereszchuk, K. A., Walker, K. A., Weaver, D., Whaley, C., and Young, J. C. (2013). Quantifying the impact of boreal forest fires on tropospheric oxidants over the atlantic using aircraft and satellites (bortas) experiment: design, execution and science overview. *Atmospheric Chemistry and Physics*, 13(13):6239–6261.

Parrington, M., Palmer, P. I., Lewis, a. C., Lee, J. D., Rickard, a. R., Di Carlo, P., Taylor, J. W., Hopkins, J. R., Punjabi, S., Oram, D. E., Forster, G., Aruffo, E., Moller, S. J., Bauguitte, S. J.-B., Allan, J. D., Coe, H., and Leigh, R. J. (2013). Ozone photochemistry in boreal biomass burning plumesParrington, M., Palmer, P. I., Lewis, a. C., Lee, J. D., Rickard, a. R., Di Carlo, P., ... Leigh, R. J. (2013). Ozone photochemistry in boreal biomass burning plumes. Atmospheric Chemistry and Physics, 13. *Atmospheric Chemistry and Physics*, 13(15):7321–7341.

Parrish, D. D., Stohl, a., Forster, C., Atlas, E. L., Blake, D. R., Goldan, P. D., Kuster, W. C., and de Gouw, J. a. (2007). Effects of mixing on evolution of hydrocarbon ratios in the troposphere. *Journal of Geophysical Research*, 112(D10):D10S34.

Petters, M. D., Carrico, C. M., Kreidenweis, S. M., Prenni, A. J., DeMott, P. J., Collett, J. L., and Moosmüller, H. (2009). Cloud condensation nucleation activity of biomass burning aerosol. *Journal of Geophysical Research*, 114(D22):D22205.

Petters, M. D. and Kreidenweis, S. M. (2007). A single parameter representation of hygroscopic growth and cloud condensation nucleus activity. *Atmospheric Chemistry and*

Physics, 7(8):1961–1971.

Pierce, J. R. and Adams, P. J. (2009). Uncertainty in global CCN concentrations from uncertain aerosol nucleation and primary emission rates. *Atmospheric Chemistry and Physics*, 9(4):1339–1356.

Pierce, J. R., Chen, K., and Adams, P. J. (2007). Contribution of primary carbonaceous aerosol to cloud condensation nuclei: processes and uncertainties evaluated with a global aerosol microphysics model. *Atmospheric Chemistry and Physics*, 7:5447–5466.

Reddington, C. L., Carslaw, K. S., Spracklen, D. V., Frontoso, M. G., Collins, L., Merikanto, J., Minikin, a., Hamburger, T., Coe, H., Kulmala, M., Aalto, P., Flentje, H., Plass-Dülmer, C., Birmili, W., Wiedensohler, a., Wehner, B., Tuch, T., Sonntag, a., O'Dowd, C. D., Jennings, S. G., Dupuy, R., Baltensperger, U., Weingartner, E., Hansson, H.-C., Tunved, P., Laj, P., Sellegri, K., Boulon, J., Putaud, J.-P., Gruening, C., Swietlicki, E., Roldin, P., Henzing, J. S., Moerman, M., Mihalopoulos, N., Kouvarakis, G., Ždímal, V., Zíková, N., Marinoni, a., Bonasoni, P., and Duchi, R. (2011). Primary versus secondary contributions to particle number concentrations in the European boundary layer. *Atmospheric Chemistry and Physics*, 11(23):12007–12036.

Reid, J., Hobbs, P., and Ferek, R. (1998). Physical, chemical, and optical properties of regional hazes dominated by smoke in Brazil. *Journal of Geophysical Research*, 103(98).

Reid, J. S., Hyer, E. J., Prins, E. M., Westphal, D. L., Zhang, J., Wang, J., Christopher, S. a., Curtis, C. a., Schmidt, C. C., Eleuterio, D. P., Richardson, K. a., and Hoffman, J. P. (2009). Global Monitoring and Forecasting of Biomass-Burning Smoke: Description of and Lessons From the Fire Locating and Modeling of Burning Emissions (FLAMBE) Program. *IEEE Journal of Selected Topics in Applied Earth Observations and Remote Sensing*, 2(3):144–162.

Reid, J. S., Koppmann, R., Eck, T. F., and Eleuterio, D. P. (2005). A review of biomass burning emissions part II: intensive physical properties of biomass burning particles. *Atmospheric Chemistry and Physics*, 5(3):799–825.

Rissler, J., Vestin, A., Swietlicki, E., Fisch, G., Zhou, J., Artaxo, P., and Andreae, M. O. (2006). Size distribution and hygroscopic properties of aerosol particles from dry-season biomass burning in Amazonia. *Atmospheric Chemistry and Physics*, 6:471–491.

Sakamoto, K. M., Allan, J. D., Coe, H., Taylor, J. W., Duck, T. J., and Pierce, J. R. (2014). Aged boreal biomass burning aerosol size distributions from bortas 2011. *Atmospheric Chemistry and Physics Discussions*, 14(17):24349–24385.

Seinfeld, J. H. and Pandis, S. N. (2006). *Atmospheric Chemistry and Physics*. Wiley.

Spracklen, D. V., Carslaw, K. S., Pöschl, U., Rap, a., and Forster, P. M. (2011). Global cloud condensation nuclei influenced by carbonaceous combustion aerosol. *Atmospheric Chemistry and Physics*, 11(17):9067–9087.

Staudt, A. C., Jacob, D. J., Logan, J. A., and Sachse, G. W. (2001). Continental sources , transoceanic transport , and interhemispheric exchange of carbon. 106(April 1999).

Stevens, R. G. and Pierce, J. R. (2013). A parameterization of sub-grid particle formation in sulfur-rich plumes for global- and regional-scale models. *Atmospheric Chemistry and Physics*, 13(23):12117–12133.

Stevens, R. G. and Pierce, J. R. (2014). The contribution of plume-scale nucleation to global and regional aerosol and CCN concentrations: evaluation and sensitivity to emissions changes. *Atmospheric Chemistry and Physics Discussions*, 14(15):21473–21521.

Stevens, R. G., Pierce, J. R., Brock, C. A., Reed, M. K., Crawford, J. H., Holloway, J. S., Ryerson, T. B., Huey, L. G., and Nowak, J. B. (2012). Nucleation and growth of sulfate aerosol in coal-fired power plant plumes: sensitivity to background aerosol and meteorology. *Atmospheric Chemistry and Physics*, 12(1):189–206.

Stuart, G. S., Stevens, R. G., a. I. Partanen, Jenkins, a. K. L., Korhonen, H., Forster, P. M., Spracklen, D. V., and Pierce, J. R. (2013). Reduced efficacy of marine cloud brightening geoengineering due to in-plume aerosol coagulation: parameterization and global implications. *Atmospheric Chemistry and Physics*, 13(20):10385–10396.

Taylor, J. W., Allan, J. D., Allen, G., Coe, H., Williams, P. I., Flynn, M. J., Le Breton, M., Muller, J. B. a., Percival, C. J., Oram, D., Forster, G., Lee, J. D., Rickard, a. R., and Palmer, P. I. (2014). Size-dependent wet removal of black carbon in Canadian biomass burning plumes. *Atmospheric Chemistry and Physics Discussions*, 14(13):19469–19513.

van der Werf, G. R., Randerson, J. T., Giglio, L., Collatz, G. J., Mu, M., Kasibhatla, P. S., Morton, D. C., DeFries, R. S., Jin, Y., and van Leeuwen, T. T. (2010). Global fire emissions and the contribution of deforestation, savanna, forest, agricultural, and peat fires (19972009). *Atmospheric Chemistry and Physics*, 10(23):11707–11735.

Whitby, E., McMurry, P., Shankar, U., and Binkowski, F. S. (1991). Modal aerosol dynamics modeling. Technical report, Office of research and development U.S. environmental protection agency.

Wiedensohler, A. (1988). An approximation of the bipolar charge distribution for particles in the submicron size range. *Journal of Aerosol Science*, 19(3):387 – 389.

Wiedinmyer, C., Akagi, S. K., Yokelson, R. J., Emmons, L. K., Al-Saadi, J. a., Orlando, J. J., and Soja, a. J. (2011). The Fire INventory from NCAR (FINN): a high resolution global model to estimate the emissions from open burning. *Geoscientific Model Development*, 4(3):625–641.

Yokelson, R. J., Crounse, J. D., Decarlo, P. F., Karl, T., Urbanski, S., Atlas, E., Campos, T., and Shinozuka, Y. (2009). Emissions from biomass burning in the Yucatan. *Atmospheric Chemistry and Physics*, pages 5785–5812.

Appendix A: Supplementary Material to Chapter 2

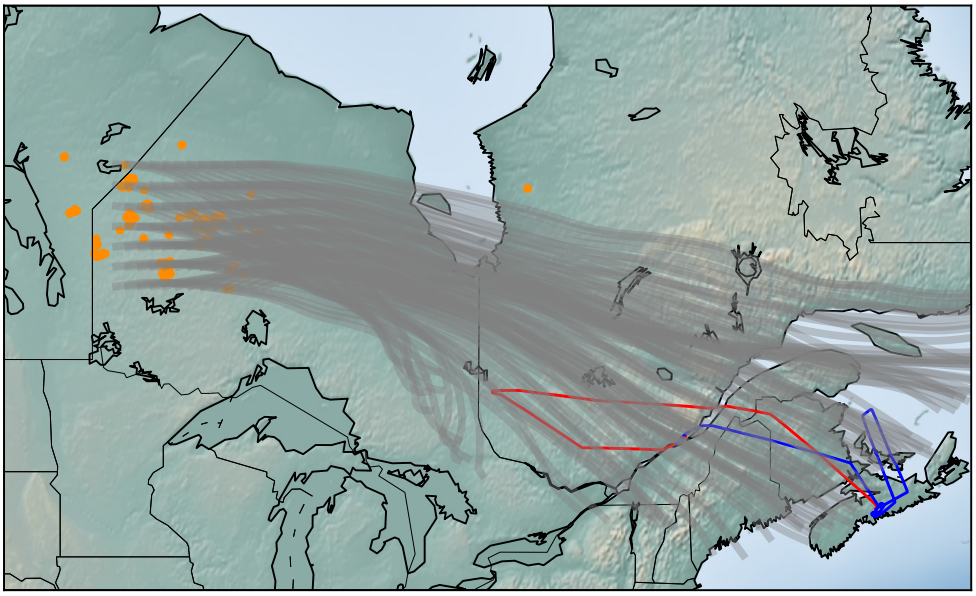

FIGURE A.1. Matrix HYSPLIT trajectories from the region over the source fires (43°–54° N, 55°–94° W, starting altitude = 1000 m) for 48 hours beginning July 18th, 2011. Fires from MODIS with radiative fire power >100 MW are seen in orange for July 17th, 2011. Analysed research flight paths on July 20th, 2011 are seen in red (b622) and blue (b623). The trajectories show smoke being transported eastward towards the sampling flights. Altitudes of the trajectories vary between 700 m – 5 km.

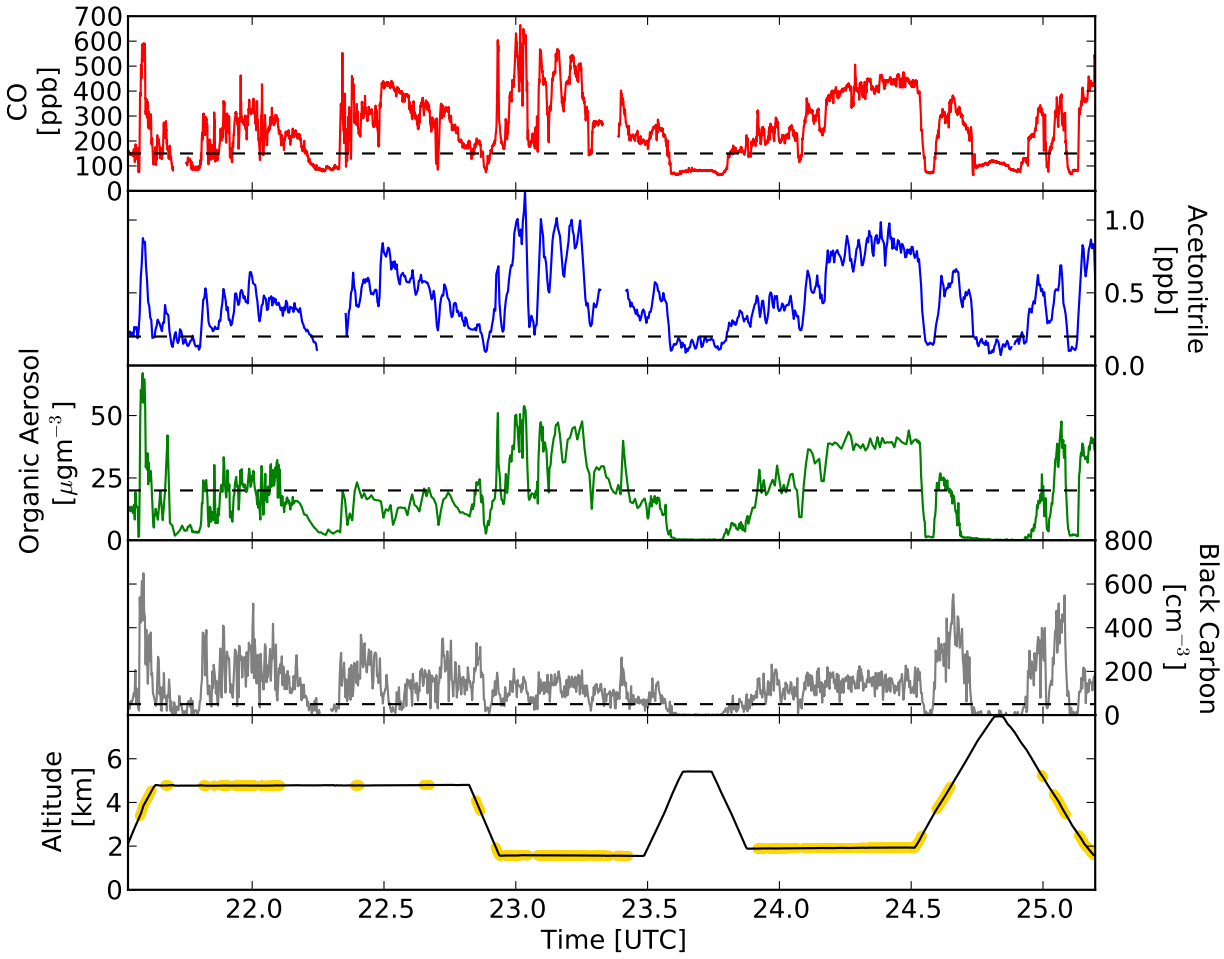

FIGURE A.2. Time series of BORTAS-B aircraft measurements of biomass-burning tracer species for Flight b623. Threshold values were used across four species as plume criteria: i) CO (red, threshold = 150 ppb), ii) Acetonitrile (blue, threshold = 200 pptv), iii) Organic aerosols (green, mass threshold= 20 μg m^{-3}, at STP), iv) Black carbon (grey, number threshold = 50 cm^{-3}, at STP). The bottom panel shows flight altitude with plume sampling periods coloured (gold).

$$K_{12} = 2\pi(D_1 + D_2)(D_{p1} + D_{p2}) \left(\frac{(D_{p1} + D_{p2})}{D_{p1} + D_{p2} + 2(g_1^2 + g_2^2)^{\frac{1}{2}}} + \frac{8(D_1 + D_2)}{(D_{p1} + D_{p2})(\bar{c}_1^2 + \bar{c}_2^2)^{\frac{1}{2}}} \right)^{-1}$$

where

$$\bar{c}_i = \left(\frac{8kT}{\pi m_i} \right)^{\frac{1}{2}} \qquad g_i = \frac{(D_{pi} + l_i)^3 - (D_{pi}^2 + l_i^2)^{\frac{3}{2}}}{3 D_{pi} l_i} - D_{pi}$$

$$l_i = \frac{8 D_i}{\pi \bar{c}_i} \qquad D_i = \frac{kTC_c}{3\pi\mu D_{pi}}$$

Variable definitions:

D_{pi} = diameter of particle i, m

D_i = Brownian diffusion coefficient of particle i,

g_i = mean particle distance after l_i, m

l_i = mean free path, m

C_c = slip correction, unitless

μ = viscosity of air, kg m^{-1} s^{-1}

$\bar{c}_i$ = mean thermal speed, m s^{-1}

T = temperature, K

m_i = mass of particle i, kg

k = Boltzmann constant, JK^{-1}

FIGURE A.3. Fuchs form of the brownian coagulation coefficient K_{12}. Taken from Seinfeld and Pandis (2006).

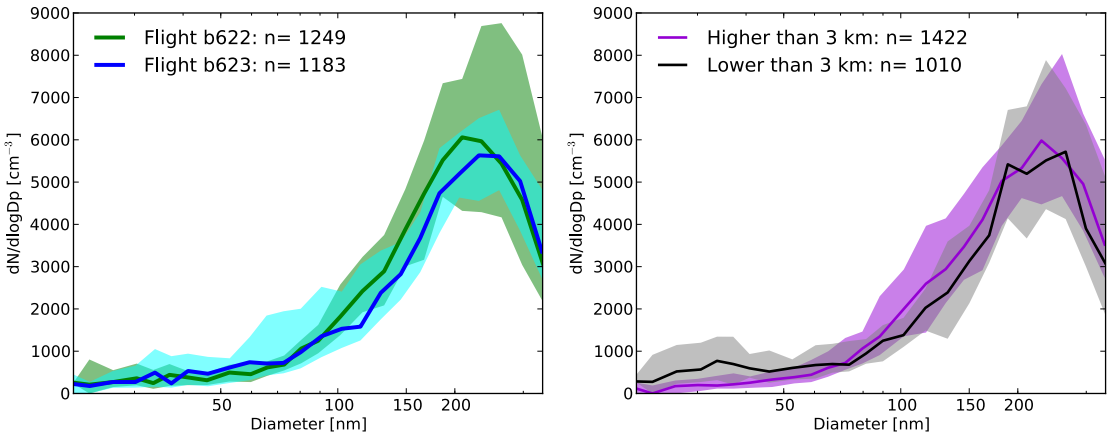

FIGURE A.4. SMPS plume size distributions showing the median and 25th and 75th percentiles by a) flight (left) and b) altitude (right).

Appendix B: Supplementary Material to Chapter 3

$$D_{pm} = \bar{M}_{k_1}^{\hat{k_1}} \bar{M}_{k_2}^{\hat{k_2}}$$
$$ln^2\sigma = \frac{2}{k_1 - k_2} ln\left(\frac{\bar{M}_{k_1}}{\bar{M}_{k_2}^r}\right)$$

where for $k_1 = 0$ and $k_2 = 3$:

$$M_0 = \int d_p^0 n(d_p)\,\mathrm{d}d_p = N \qquad M_3 = \int d_p^3 n(d_p)\,\mathrm{d}d_p = \tfrac{6}{\pi} V$$

Variable definitions:

$$r = \tfrac{k_1}{k_2} \qquad \bar{M}_k = \tfrac{M_k}{N}$$
$$\hat{k_1} = \tfrac{1}{r(k_2 - k_1)} \qquad \hat{k_2} = \tfrac{r}{k_1 - k_2}$$

FIGURE B.1. Calculation of lognormal D_{pm} and σ from two moments of a size-distribution mode. Taken from Whitby et al. (1991).

FIGURE B.2. Fortran90 code from GEM-SA to run the emulator offline. The code takes the GEM-SA built emulator parameter files and generates the output estimates from an emulator input file.

```
MODULE EMULATOR
real, allocatable :: xmod(:,:), ainv(:,:), g(:), ainvh(:,:), inv_hainvh(:,:)
real, allocatable :: h(:), betahat(:), roughness(:), min(:), max(:), t(:), ainvt(:)
real, allocatable :: tainvh(:), hdiff(:), xpred(:)
real prec, scalemean, scalesd
integer nmod, nreg, ninputs
END MODULE EMULATOR

PROGRAM MAIN_EMULATOR
implicit none
integer i, npred
real x, sd

!open file for emulator prediction inputs
OPEN(UNIT=22, FILE='emulator_inputs.txt', status='old')
read(22,*)npred

!open file for emulator prediction outputs
OPEN(UNIT=23, FILE='emulator_outputs.txt', status='replace')
CALL INIT() ! reads emulator information from files

!write header on outputs file
write(23,*)' point ',' estimate ',' std.deviation '

x = 0.
DO i = 1, npred
CALL NEXTPOINT(x,sd) ! read next prediction point from file and evaluate emulator at
that point.
write(*,*) x, sd
write(23, *) i, x, sd
ENDDO

DO i=20,31
CLOSE(i)
ENDDO
END
!_____**

SUBROUTINE INIT()
! open files, read data
```

```
USE EMULATOR

implicit none
integer i, j

!open emulator setup files
OPEN(UNIT=20, FILE='emulator_ainv.txt', status='old') ! inverse correlation matrix
OPEN(UNIT=21, FILE='emulator_training_inputs.txt', status='old') ! training data inputs
OPEN(UNIT=24, FILE='emulator_mu_out.dat', status='old') ! estimated regression parameters
OPEN(UNIT=25, FILE='emulator_precision_out.dat', status='old') ! estimated GP prec = 1/variance
OPEN(UNIT=26, FILE='emulator_ainvh.txt', status='old') ! ainv.H
OPEN(UNIT=27, FILE='emulator_rough_out.dat', status='old') ! estimated function roughnesses
OPEN(UNIT=28, FILE='emulator_g.txt', status='old') ! ainv.(y-Hb)
OPEN(UNIT=29, FILE='emulator_inv_hainvh.txt', status='old') ! (H'.ainv.H)^-1
OPEN(UNIT=30, FILE='emulator_minmax.txt', status='old') ! maxs and mins of each input
OPEN(UNIT=31, FILE='emulator_scale.txt', status='old') ! mean and sd of output scaling

read(21,*)nmod, ninputs, nreg
ALLOCATE(h(nreg), t(nmod), min(ninputs), max(ninputs), ainv(nmod,nmod),
xmod(nmod,ninputs), ainvh(nmod,nreg), betahat(nreg), roughness(ninputs), g(nmod),
inv_hainvh(nreg,nreg), ainvt(nmod),tainvh(nreg), hdiff(nreg), xpred(ninputs))

read(30,*)(min(i), i=1, ninputs)
read(30,*)(max(i), i=1, ninputs)
read(31,*)scalemean, scalesd

DO i = 1, nmod
read(20,*)(ainv(i,j), j = 1, nmod)
read(21,*)(xmod(i,j), j = 1, ninputs)
read(26,*)(ainvh(i,j), j = 1, nreg)
ENDDO

read(24,*)(betahat(i), i=1, nreg)
read(25,*)prec
read(27,*)(roughness(i), i=1, ninputs)
read(28,*)(g(i), i=1, nmod)

DO i = 1, nreg
read(29,*)(inv_hainvh(i, j), j = 1, nreg)
ENDDO
```

```
RETURN

END !-----------------------------------------------------
SUBROUTINE NEXTPOINT(x, sd)
! reads next emulator prediction input and evaluates the emulator at that point
! mean and standard deviation returned through x and sd
USE EMULATOR

implicit none
integer i
real x, sd, aux
! read next point into xpred
read(22,*)(xpred(i), i=1, ninputs)
! rescale inputs exactly as in the emulator building code
xpred = (xpred - min)/(max-min)
h(1) = 1.
IF (nreg.gt.1) THEN
DO i=1, ninputs
h(i+1) = xpred(i) ! assumes linear regression terms only
ENDDO
ENDIF
! compute t vector of correlations between xpred and training data inputs
DO i=1, nmod
t(i) = exp(-SUM(roughness*(xpred-xmod(i,:))*(xpred-xmod(i,:))))
ENDDO
! compute mean
x = scalemean + scalesd*(DOT_PRODUCT(h, betahat) + DOT_PRODUCT(t, g))
! compute standard deviation
ainvt = MATMUL(ainv, t)
tainvh = MATMUL(t, ainvh)
hdiff = h - tainvh
aux = (1.0 - DOT_PRODUCT(t, ainvt) + DOT_PRODUCT(hdiff, MATMUL(inv_hainvh,
hdiff)))/prec
IF (aux .le. 0.) THEN
sd = 0.
ELSE
sd = scalesd*SQRT(aux)
ENDIF
RETURN

END !-----------------------------------------------------
```

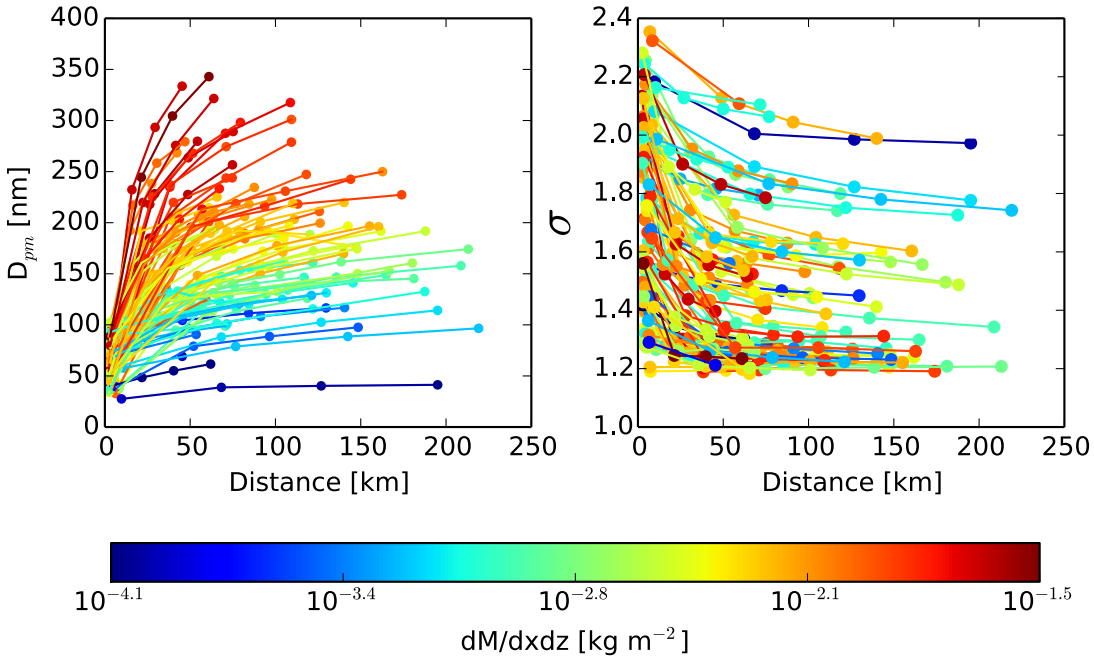

FIGURE B.3. Wire plots showing size-distribution changes across individual SAM-TOMAS simulations coloured by dM/dxdz for D_{pm} (left) and σ (right).

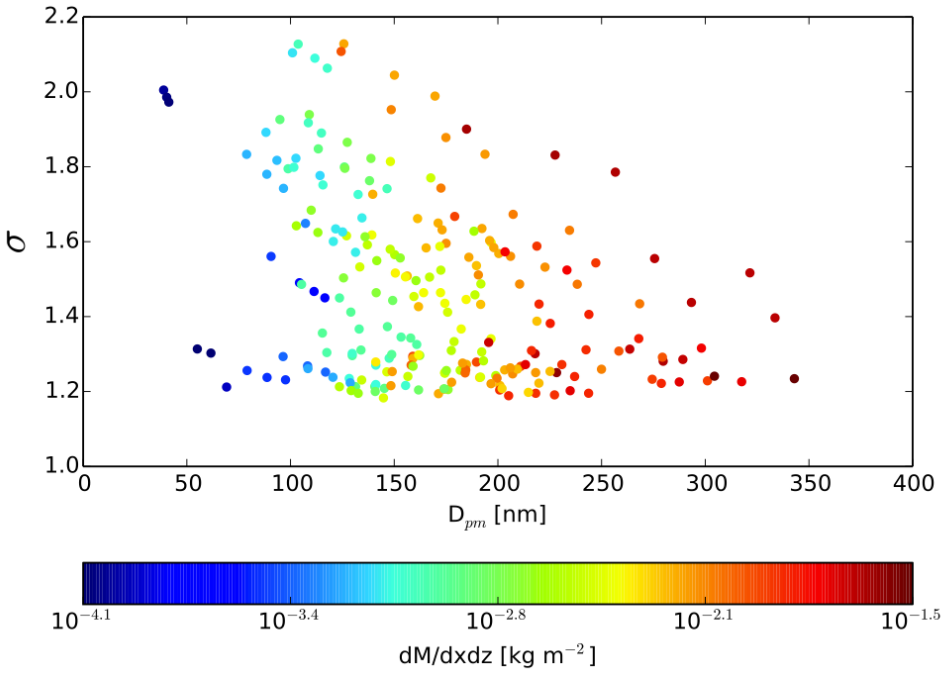

FIGURE B.4. Scatter plot showing the relationships between final modal width (σ), final D_{pm}, and dM/dxdz (total mass of emissions normalized to SAM x-gridbox and z-gridbox) for each of the 400 simulation slices. The data are filtered for distances >25 km to minimize the influence of the initial size-distribution parameters.

$$\text{MNB} = \frac{1}{N} \sum \frac{C_m - C_o}{C_o}$$

FIGURE B.5. Mean normalized bias equation. N is the number of data points, C_m is the modelled data and C_o is the 'observation' data (in this study, the SAM-TOMAS data).